

Teze disertace
k získání vědeckého titulu "doktor věd"
ve skupině věd technické

Název disertace:
Multiscale hierarchical modeling of hydrating concrete

Komise pro obhajoby doktorských disertací v oboru: Mechanika pevných těles

Jméno uchazeče: Doc. Ing. Vít Šmilauer, Ph.D.

Pracoviště uchazeče: ČVUT v Praze, Fakulta stavební

Místo a datum: Praha, 12. listopadu 2017

Contents

1	Summary	3
2	Introduction	5
2.1	Challenges in structural concrete	6
3	Multiscale modeling approach	7
4	Cement hydration models	10
4.1	CEMHYD3D hydration model	10
4.2	Affinity hydration models	11
5	Elastic homogenization of cement composites	12
5.1	Continuum micromechanical methods	13
5.2	Numerical homogenization methods	15
5.3	Paste of Kamali et al., w/c = 0.5	16
5.4	Analytical approximation of Young's modulus	16
6	Identification of non-aging basic C-S-H creep	17
6.1	Visco-elastic homogenization via FFT-based method	19
6.2	Inverse creep analysis for two-year old cement paste	20
6.3	Long-term creep upscaled to the concrete level	22
7	Multiscale simulation of heat transport	23
7.1	Mathematical formulation of heat transport	23
7.2	Space and time discretization	25
7.3	Validation	26
7.3.1	Temperature evolution on a prestressed bridge	26
7.3.2	Optimal position of cooling pipes	30
7.3.3	Further validations for concrete temperatures	31
8	Conclusions	34
9	Acknowledgement	34
10	References	34

1 Summary

The thesis focuses on multiscale hierarchical modeling of hydrating concrete. Concrete is the most man-made material in the world, annually exceeding 1.5 cubic meter for every person on the Earth. Concrete represents a multiscale material, spanning lengths from atomic scale to tenths of meters. Nowadays, its production utilizes cement, water, fine aggregates, coarse aggregates, admixtures, and supplementary cementitious materials which extends material complexity even further. Besides that, concrete often takes a shape of structural elements, adding structural scale to the material.

Recent advances in experimental and numerical techniques during the last decades helped us to step down on sub-micrometer scale. The thesis demonstrates four areas where multiscale approach brings new insight and predictive capabilities:

- Hydration models - Section 4
- Elasticity - Section 5
- Viscoelasticity - Section 6
- Heat transport - Section 7

Hydration models are presented by CEMHYD3D and affinity models, calibrated for experimental data. Their performance is validated by means of isothermal calorimetry. Both models show excellent prediction for hydration heat and volume phases during hydration. CEMHYD3D provides 3D microstructure of cement paste at the resolution of 1 μm , suitable for further numerical homogenization techniques.

Elasticity evolution during concrete hydration is explored using continuum and numerical micromechanics. The concept of strain localization in heterogeneous microstructure leads to bounds and estimates. Eshelby's finding that strain remains constant in ellipsoidal inclusions led to Mori-Tanaka and self-consistent schemes. Numerical methods are represented by finite elements and FFT-based methods on periodic microstructures.

Creep is explored by means of downscaling to identify intrinsic creep of C-S-H. A macroscopic B3 creep model is recalibrated for C-S-H, showing much larger creep on C-S-H scale than on the cement paste. FFT-based method is extended for viscoelastic homogenization and continuum micromechanics transfers C-S-H creep to the scale of concrete.

Heat transport and temperature rise in hydrating concrete belongs to classical challenges in massive concrete structures. This task was formulated as a multiscale problem where predicted released heat from the scale of cement paste is upscaled to the scale of structure. Since the coupling is nonlinear, numerical solution is employed on both scales. Several validations show excellent temperature predictions in various concrete mix designs. This multiscale model

was further incorporated into ConTemp - A virtual thermo-mechanical simulator for hydrating reinforced concrete blocks. Currently, the tool is used in 20 countries around the world by LafargeHolcim company, assisting in mix design and optimization of massive concrete by engineers.

Extension to localized phenomena, such as strength predictions, presents a challenging task due to strain localization on different scales. Accessing strength properties on a sub-micrometer scale and formulating multiscale models belong to current research activities.

2 Introduction

Concrete is the most produced man-made material in the world, annually exceeding 1.5 cubic meter for every person on the Earth. Fig. 1 compares concrete production with other common materials in the world, showing its dominant role.

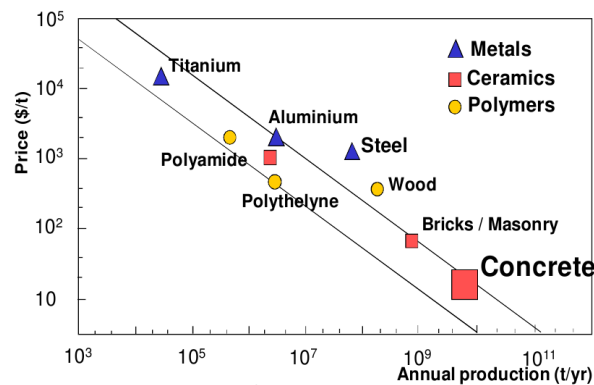


Figure 1: Annual production and price for common materials in 1990's [35]

The term “concrete” symbolizes a wide range of composite materials having normally compliant matrix (chemically based on calciumsilicates, aluminosilicates, asphalt, sulphur etc.) with stiff inclusions (aggregates, fillers). The thesis focuses further mainly on the matrix derived from Portland cement (calcium-silicates), which constitutes the most common building material used today in civil engineering. The majority of chemical and mechanical changes occur during maturing, or hydration, which controls final properties of concrete.

A brief history of concrete ancestors starts with Assyrians, Babylonians, Chinese and Egyptians who used clay or lime materials several thousands years BC. Around 200 BC, the Romans started to use pozzolanic volcanic ash which significantly improved material durability and such material had hardened under water. Little progress occurred during the middle ages until the mid of 18th century, when John Smeaton from England discovered excellent properties of cement made from clay-rich limestone. He rebuilt Eddystone Lighthouse in Cornwall, England. Vicat prepared artificial hydraulic lime in 1812-13 from synthetic mixture of limestone and clay.

Contemporary concrete stems from Joseph Aspdin's patent from 1824. He patented Portland cement, named after the building stones quarried at Portland, England. Joseph Monier reinforced flower pots in 1867 with iron bars, laying foundations for reinforced concrete. In 1887, Henri Le Chatelier established oxide ratios for proper dosing of lime to produce Portland cement. He is considered a founder of modern cement chemistry. The gypsum was introduced in 1890 in the USA to act as a retardant of concrete setting. In 1930, the entrained air was firstly used to decrease freeze-thaw damage.

In 1940's Powers and Brownard formulated macroscopic hydration model that was able to quantify hydration products and separate non-evaporable, gel, and capillary water in the matrix [43]. Neville summarized the comprehensive knowledge about concrete in his famous book in 1963, reprinted and extended several times [38]. Lea from 1935 and Taylor from 1963 summarized knowledge of cement chemistry resulting in other well-known books, several times reprinted [32, 59]. The silica fume, as a pozzolanic additive, and superplasticizers were introduced in 1980's.

Scientific and technological efforts, since patenting Portland cement in 1824, resulted in a deeper understanding of contemporary concrete and in mastering its production and technology. Developments in the last 50 years have brought a common use of plasticizers, admixtures and supplementary cementitious materials, which gave birth to high performance concretes. These high-tech and fire-resistant materials started replacing steel columns in skyscrapers, unimaginable just 50 years ago.

2.1 Challenges in structural concrete

Extensive application of concrete worldwide revealed several problems associated with a lack of fundamental knowledge on different scales. Common areas of challenges include:

Heat of hydration as the result of exothermic chemical reactions. Since heat energy dissipation approximately relates to the square of specimen's size, temperature rise presents a serious problem in massive structures where dimensions exceed approximately 0.5 m and where cracks easily form during a cooling stage.

Slow strength evolution in blended systems made from Portland clinker and supplementary cementitious materials (SCMs) such as slag, fly ash, calcined clay, or other byproducts. The reactivity of SCMs is usually low and strength gain delayed.

Concrete creep plays role in long-term performance of structures (bridge deflection, prestress loss, shortening of columns in high-rise buildings). It has been found that concrete creep cannot be simply assessed with accelerated laboratory tests and to cover easily wide variations in concrete composition [45].

Reinforcement corrosion due to a loss of alkaline concrete environment or ingress of aggressive ions. Carbonation and chloride ingress represent the most common processes leading to the corrosion of reinforcing steel. The induction period is largely influenced by matrix porosity, its chemical composition and cracks in the cover layer of concrete.

Reduced creep and ductility caused by increased concrete strength. Brittleness is generally proportional to the square of tensile strength. In applications controlled by deformations (drying shrinkage, temperature, slabs on elastic foundations), stronger concrete withstands generally lower deformation due to steeper strain softening curve, leading to cracking.

Multiscale methods can tackle those challenges from experimental and numerical modeling. From the pioneering work “Numerical concrete” by Roelfstra [46], many scientists and organizations followed multiscale simulations, such as the Virtual Cement and Concrete Testing Laboratory at the National Institute of Standards and Technology (NIST), USA [10], or DuCOM platform for simulating concrete durability [34], to mention a few.

3 Multiscale modeling approach

Multiscale methods exploit the fact that different mechanisms or morphologies may exist on different scales of observation. Material heterogeneity is often encountered, either in a form of chemically distinct materials or of the same material in different states such as polycrystals. Concrete is a typical representative of multiscale materials, in which well-established scales span at least eight orders of magnitude. The complexity of cement-based materials is demonstrated in Fig. 2 in various morphologies and scales.

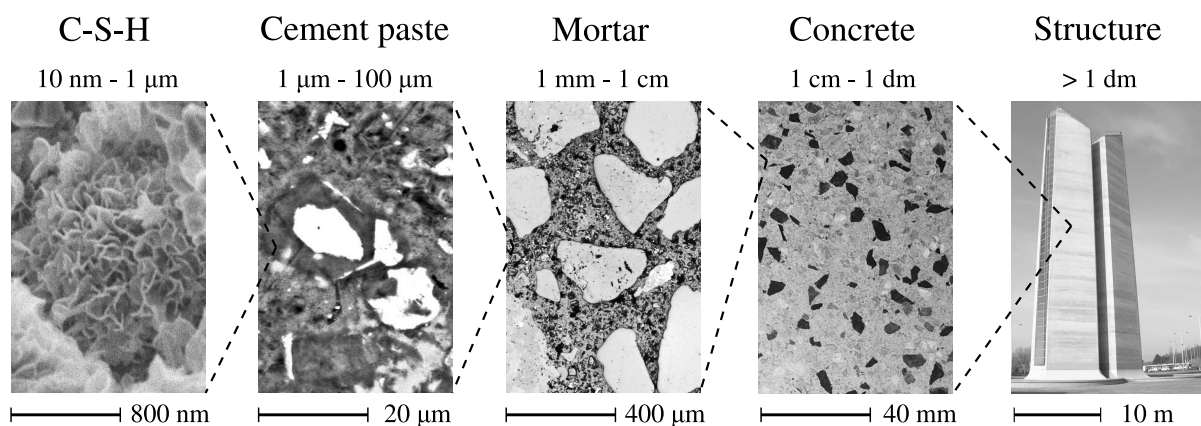


Figure 2: Multiscale nature of concrete. Images by L. Kopecký (CTU in Prague) and M.K. Head (Imperial College London).

Scale separation in heterogeneous materials can be introduced in many ways. For the case of cement-based materials, five levels were generally accepted, originating from a coincidence with experimental techniques applied[12]:

C-S-H level typically spans a characteristic length between 10 nm – 1 μm . At least two morphologies of C-S-H_{LD} and C-S-H_{HD} were identified.

Cement paste level is found on a resolution between 1 μm – 100 μm . Clinker minerals, gypsum, CH, homogenized C-S-H and some capillary porosity are recognizable at this resolution [12].

Mortar level is considered on a scale between 1 mm and 1 cm. It contains homogenized cement paste, fine aggregates such as sand and associated ITZ. Air voids may be present as well.

Concrete level spans, in a typical structural concrete, a characteristic length of 1 cm – 1 dm. Homogenized mortar, coarse aggregates such as gravel, and associated ITZ are typically observed.

Structural level represents a structural element in the shape of column, beam, or slab. These elements have dimensions typically above 1 dm. Structural engineers are familiar with this level, where concrete is treated as a continuum. The structural level addresses real environmental boundary conditions.

Generally, multiscale methods aim at data transfer across scales. Depending on a solution strategy, the multiscale methods are classified into two broad groups. *Hierarchical methods* represent the first category and originate from three assumptions; scale separation, uniformity of the macroscopic field in the vicinity of a material point, and local periodicity, see Fig. 3.

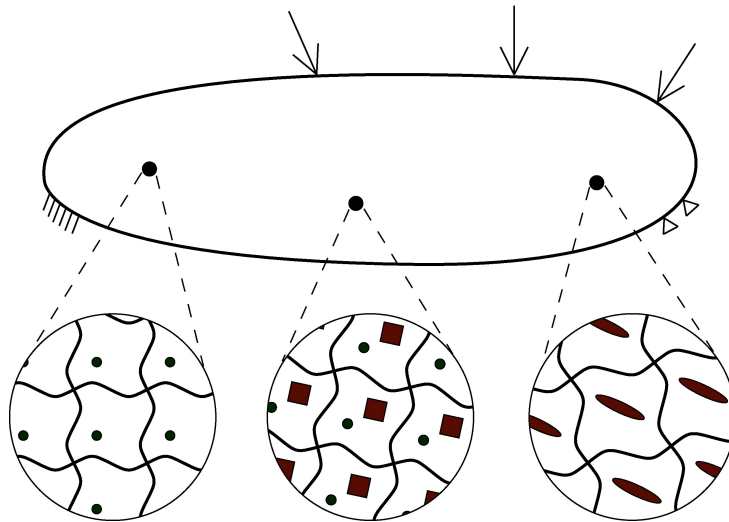


Figure 3: Local periodicity and different volume elements in the vicinity of material points.

The solution proceeds from a value of the macroscopic field, which is passed to the lower scale where it is used to establish the boundary conditions of the microproblem. Homogenization of the microproblem yields an effective property, which is passed back to the material point

on a higher scale. The material point often corresponds to the integration point of FE. At the end, sequential processing of many sub-problems leads to the solution of the macroproblem. The scheme is often enhanced with iterations between scales so equilibrium is reached on both scales.

Hierarchical methods are perfectly suited to the prediction of non-localized phenomena, such as elasticity or hardening plasticity [11, 18, 31]. Predictive capabilities can be extended when macro-field gradients also are transferred to the microscale [31]. On the other hand, hierarchical methods are generally unjustified for the prediction of the softening fracturing behavior. Complications arise due to the fact that damage localization and the associated material characteristic length on both the macroscale and subscale become easily incompatible with the imposed boundary conditions. Localization limiters, such as the crack band of the non-local approach, bring a remedy, but weaken the predictive capabilities of such multiscale simulations.

In the hierarchical methods, the bridging of adjacent scales may be chained many times over, as demonstrated in Fig. 2. Depending on the direction of the scale transfer, two strategies are commonly used:

Upscaling of constituent properties from a lower to a higher scale. Data from the lower scale are compressed into effective properties. For example, the elasticity of mortar has its origin in the cement paste and fine aggregates. Thus combining these two materials together results in an effective mortar property.

Downscaling occurs less frequently and implies data acquisition. Knowing a macroscale property raises the question of how each constituent contributes. A typical example is the inverse analysis of C-S-H creep from creep tests. Once the assumption that creep localizes in C-S-H is adopted, one aims to filter out the elastic components within the cement paste and thus to identify intrinsic C-S-H creep. Under normal circumstances, only average properties are identified.

The second group, known as *concurrent methods*, apply substructuring techniques which lead to one simultaneous solution of all equations [44, 19, 23, 57, 26]. These can be decomposed further for multiple processing, known as domain-decomposition methods [17, 64]. A typical example of a concurrent method is the analysis of a cracking body, where large macroscale elements are replaced with the underlying microstructure based on crack propagation. In this method, the regions of interest are captured with sufficient microstructural details while large macroscale elements substitute distant areas [55].

4 Cement hydration models

Cement hydration models play important part in multiscale simulation of hydrating concrete on the scale of cement paste. They generally predict degree of hydration, volumetric evolution of phases (cement minerals, hydration products, water, capillary porosity), released heat while taking into account water availability and temperature evolution. In addition, 2D/3D models show topographical evolution of microstructure, suitable for numerical modeling.

The first consistent model of cement hydration belongs to Powers and Brownyard [43]. They set up equations for evolving chemical phases, particularly unreacted cement, f_{cem} , colloidal cement gel (consisting of mainly C-S-H), f_{gel} , and capillary porosity f_{cap} with empty pores f_{empty} . Fig. 4 displays volume fractions for water-to-cement ratios $wcr = 0.3$ and 0.5 under sealed curing conditions.

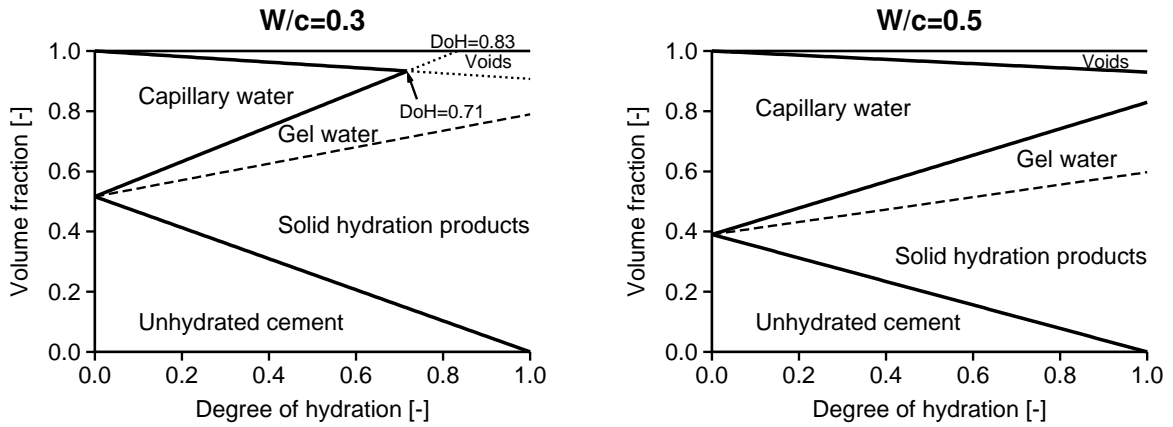
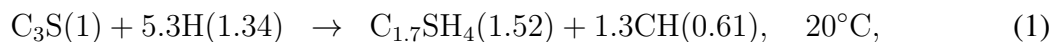


Figure 4: Evolution of chemical phases during cement hydration, for a $wcr = 0.3$ and 0.5 under sealed curing conditions. Voids correspond to chemical shrinkage. They may be resaturated when external water is available.

4.1 CEMHYD3D hydration model

CEMHYD3D represents one of the most advanced contemporary hydration models [9]. The idea is to split the cement microstructure into voxels (volume elements), typically with a size of $1 \times 1 \times 1 \mu\text{m}$. A flowchart of the CEMHYD3D model is depicted in Fig. 5, from microstructure reconstruction to predicted properties.

CEMHYD3D model implements 9 reactions, each reaction associated with enthalpy, able to predict released heat. For example, hydration of C_3S proceeds as



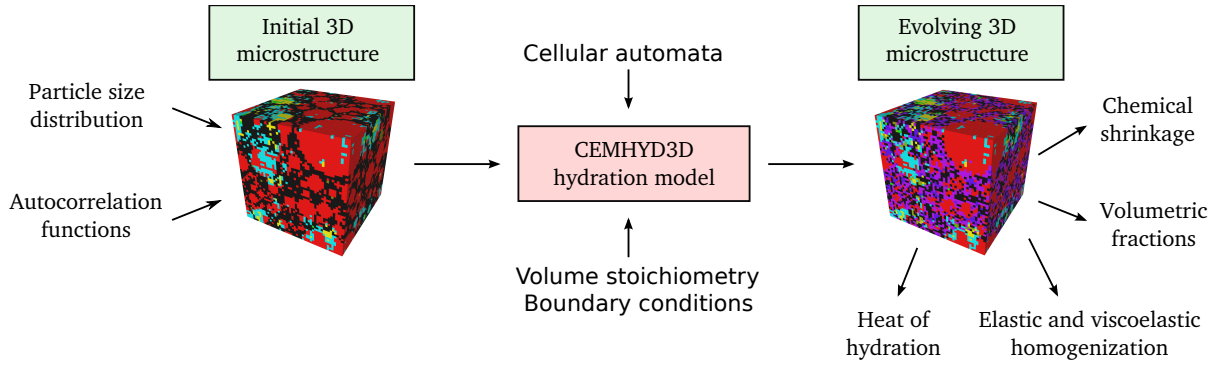


Figure 5: A flowchart of the CEMHYD3D model with consecutive outputs.

where numbers in parentheses quantify the volumetric amounts of each phase. Note 9% volume chemical shrinkage. Fig. 6 shows validation on a few Portland cements.

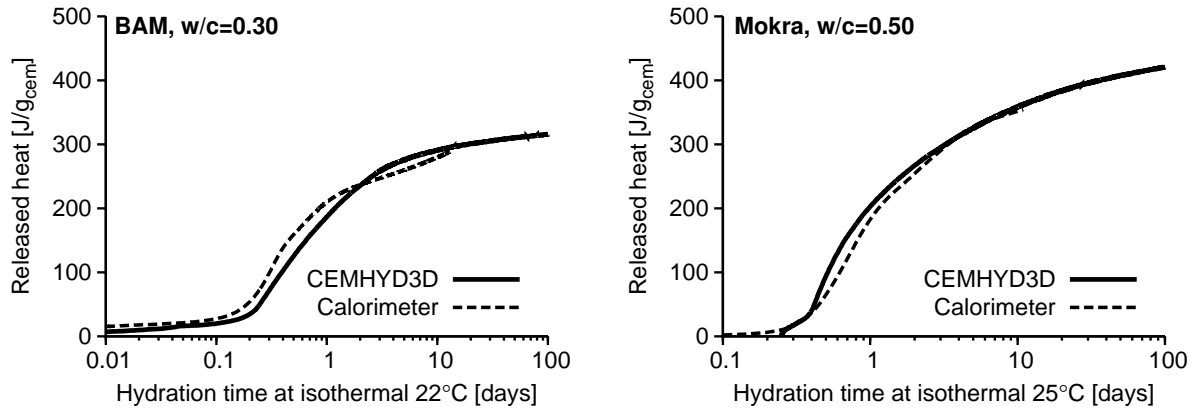


Figure 6: Validation for isothermal calorimetry in terms of released hydration heat.

4.2 Affinity hydration models

Affinity hydration models provide a phenomenological framework for accommodating all stages of cement hydration. The rate of hydration can be expressed by the temperature-independent normalized chemical affinity, $\tilde{A}_{25}(DoH)$, related to heat flow from isothermal calorimetry at 25°C as $\tilde{A}_{25}(DoH) = q(t)/Q_{pot}$

$$\frac{dDoH(T)}{dt} = \tilde{A}_{25}(DoH) \exp \left[\frac{E_a}{R} \left(\frac{1}{273.15 + 25} - \frac{1}{T} \right) \right] \quad (2)$$

where DoH is degree of hydration, Q_{pot} represents potential heat of hydration, and E is the activation energy.

Cervera *et al.* [14] proposed an analytical form of the normalized affinity which we modified further

$$\tilde{A}_{25}(DoH) = B_1 \left(\frac{B_2}{DoH_\infty} + DoH \right) (DoH_\infty - DoH) \exp \left(-\bar{\eta} \frac{DoH}{DoH_\infty} \right), \quad (3)$$

where B_1, B_2 are coefficients to be calibrated, DoH_∞ is the ultimate hydration degree and $\bar{\eta}$ represents microdiffusion of free water through formed hydrates.

The affinity hydration from Eqs. (2), (3) performs well on all Portland-based cements [48, 49]. Fig. 7 validates them graphically against isothermal calorimetry data or CEMHYD3D simulation [10].

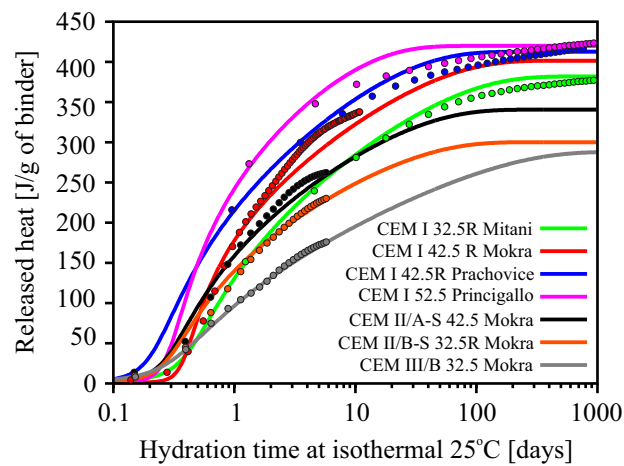


Figure 7: Validation of affinity hydration model on Portland-based cements.

5 Elastic homogenization of cement composites

This chapter explores an application of homogenization techniques to the cement paste and consecutive composites such as mortar and concrete for linear elasticity [53]. The Young's modulus is very often found to be linear with the degree of hydration, in a wide range of wcr and types of cement paste [16]. Till today, explanation and possible mechanism of this phenomenon has been proposed by only a few authors and are based only on hydrating phase [16]. The linearity is astonishing when we consider porous evolving material with the solid phases having the difference between elastic modulus by approximately 5, not talking about curing, water availability or temperature.

5.1 Continuum micromechanical methods

Continuum micromechanics rely predominantly on the concept of concentration or localization. The local stress or strain fields $\boldsymbol{\sigma}(\boldsymbol{x})$, $\boldsymbol{\epsilon}(\boldsymbol{x})$ are derived directly from the macroscopic stress $\boldsymbol{\Sigma}$ and strain \boldsymbol{E} . This problem cannot be solved in general, so an additional assumption is made which leads to an *estimate* or to a *bound*. In the case of estimates, the boundary conditions of inclusion are generally unknown, so the problem is at first transformed to the problem with homogeneous boundary conditions [22, 24]. Static uniform boundary conditions are defined as

$$\boldsymbol{p}(\boldsymbol{x}) = \boldsymbol{\Sigma} \cdot \boldsymbol{n}, \quad (4)$$

where \boldsymbol{n} is the unit normal vector pointing outwards from the boundary and \boldsymbol{p} are surface tractions. For any equilibrated stress field $\boldsymbol{\sigma}(\boldsymbol{x})$, the volume average yields back a homogeneous stress

$$\langle \boldsymbol{\sigma}(\boldsymbol{x}) \rangle = \frac{1}{V} \int_V \boldsymbol{\sigma}(\boldsymbol{x}) dV = \boldsymbol{\Sigma}. \quad (5)$$

Similarly, a macroscopic strain can be imposed through surface displacements, or kinematic uniform boundary conditions

$$\boldsymbol{u}(\boldsymbol{x}) = \boldsymbol{E} \cdot \boldsymbol{x}, \quad (6)$$

where $\boldsymbol{u}(\boldsymbol{x})$ is the microscopic displacement vector and \boldsymbol{x} determines the position. For any strain field $\boldsymbol{\epsilon}(\boldsymbol{x})$ derived from any compatible displacement field according to Eq. (6), the macroscopic strain then reads

$$\langle \boldsymbol{\epsilon}(\boldsymbol{x}) \rangle = \frac{1}{V} \int_V \boldsymbol{\epsilon}(\boldsymbol{x}) dV = \boldsymbol{E}. \quad (7)$$

The homogeneous boundary conditions according to Eqs. (4), (6) enable the use of the Hill lemma for the strain energy density, where at least the strain or stress fields satisfy the homogeneous boundary conditions

$$\langle \boldsymbol{\sigma}(\boldsymbol{x}) : \boldsymbol{\epsilon}(\boldsymbol{x}) \rangle = \langle \boldsymbol{\sigma}(\boldsymbol{x}) \rangle : \langle \boldsymbol{\epsilon}(\boldsymbol{x}) \rangle = \boldsymbol{\Sigma} : \boldsymbol{E}. \quad (8)$$

In addition, Eq. (8) is also valid for periodic boundary conditions [63]. In continuum micromechanics, the approximate microscopic stress or strain field may be linked to that on the macroscopic scale. Strain or stress localization (concentration) tensors, $\mathbf{A}(\boldsymbol{x})$ and $\mathbf{B}(\boldsymbol{x})$, couple the micro and macro scale. In the case of linear elasticity it yields

$$\boldsymbol{\epsilon}(\boldsymbol{x}) = \mathbf{A}(\boldsymbol{x}) : \boldsymbol{E}, \quad (9)$$

$$\boldsymbol{\sigma}(\boldsymbol{x}) = \mathbf{B}(\boldsymbol{x}) : \boldsymbol{\Sigma}. \quad (10)$$

Note that the spatial average of concentration tensors yields a unit tensor, according to Eqs. (5), (7)

$$\langle \mathbf{A}(\mathbf{x}) \rangle = \langle \mathbf{B}(\mathbf{x}) \rangle = \mathbf{I}. \quad (11)$$

Combining Eq. (8) with Eqs. (9), (10) yields

$$\mathbf{E} : \boldsymbol{\Sigma} = \langle \boldsymbol{\epsilon}(\mathbf{x}) : \boldsymbol{\sigma}(\mathbf{x}) \rangle = \langle \boldsymbol{\epsilon}(\mathbf{x}) : \mathbf{B}(\mathbf{x}) : \boldsymbol{\Sigma} \rangle, \quad (12)$$

$$\boldsymbol{\Sigma} : \mathbf{E} = \langle \boldsymbol{\sigma}(\mathbf{x}) : \boldsymbol{\epsilon}(\mathbf{x}) \rangle = \langle \boldsymbol{\sigma}(\mathbf{x}) : \mathbf{A}(\mathbf{x}) : \mathbf{E} \rangle. \quad (13)$$

Eqs. (12), (13) are equivalent in a heterogeneous material only in sufficiently large volume elements. If not so, the effective properties may lie far apart with a strong dependence on the applied boundary conditions [30]. Let us define local constitutive equations, relating the average microscopic strain with the microscopic stress

$$\boldsymbol{\sigma}(\mathbf{x}) = \mathbf{c}(\mathbf{x}) : \boldsymbol{\epsilon}(\mathbf{x}), \quad (14)$$

$$\boldsymbol{\epsilon}(\mathbf{x}) = \mathbf{s}(\mathbf{x}) : \boldsymbol{\sigma}(\mathbf{x}), \quad (15)$$

where $\mathbf{c}(\mathbf{x})$ and $\mathbf{s}(\mathbf{x})$ are the local stiffness and compliance tensors, respectively.

Inserting Eq. (9) into Eqs. (5), (14) and Eq. (10) into Eqs. (7), (15) leads to the effective stiffness and compliance tensors. Since a heterogeneous sample is often formed from r phases with f_r volume fractions, it is possible to replace an integral with a summation

$$\boldsymbol{\Sigma} = \langle \boldsymbol{\sigma} \rangle = \frac{1}{V} \int_V \mathbf{c}_r : \mathbf{A}_r : \mathbf{E} \, dV = \sum_r f_r \mathbf{c}_r : \mathbf{A}_r : \mathbf{E} = \mathbf{C}^{eff} : \mathbf{E}, \quad (16)$$

$$\mathbf{E} = \langle \boldsymbol{\epsilon} \rangle = \frac{1}{V} \int_V \mathbf{s}_r : \mathbf{B}_r : \boldsymbol{\Sigma} \, dV = \sum_r f_r \mathbf{s}_r : \mathbf{B}_r : \boldsymbol{\Sigma} = \mathbf{S}^{eff} : \boldsymbol{\Sigma}. \quad (17)$$

Following Eshelby's idea [15], an estimate for the strain concentration tensor \mathbf{A}_r^{est} is obtained from the solution of a matrix-inclusion problem. If an inclusion has a spherical or ellipsoidal shape and is embedded in a reference medium with the stiffness tensor \mathbf{C}_0 , the strain field $\boldsymbol{\epsilon}_r$ in the inclusion is uniform for a far imposed homogeneous strain. Such an approach leads to an estimate of elastic properties. The most common choice for the localization tensor is the Eshelbian type ellipsoidal inclusion placed in a reference medium [63]

$$\mathbf{A}_r^{est} = [\mathbf{I} + \mathbf{S}_r^{Esh} : (\mathbf{C}_0^{-1} : \mathbf{c}_r - \mathbf{I})]^{-1} : \left\langle [\mathbf{I} + \mathbf{S}_r^{Esh} : (\mathbf{C}_0^{-1} : \mathbf{c}_r - \mathbf{I})]^{-1} \right\rangle^{-1}. \quad (18)$$

Continuum homogenization methods lead to several bounds; Voight, Reuss, Hashin-Shtrikman and Walpole bounds, or estimates such as Mori-Tanaka method, and self-consistent scheme. Intrinsic elastic properties of phases can be found experimentally by nanoindentation [41, 50].

An example applicable to concrete considers the aggregate volume fraction of 0.75 embedded in a hydrating cement paste. The aggregates have constant elastic properties $E_i = 60$ GPa with $\nu_i = 0.3$ and the paste $\nu_m = 0.3$ with a varying Young's modulus from 0 to 40 GPa. Fig. 8 summarizes the performance of seven homogenization methods. It becomes evident that a lower contrast between the phases implies a lower difference in effective properties by different homogenization methods. The continuum methods formed the basis of multiscale model for alkali-activated materials [54].

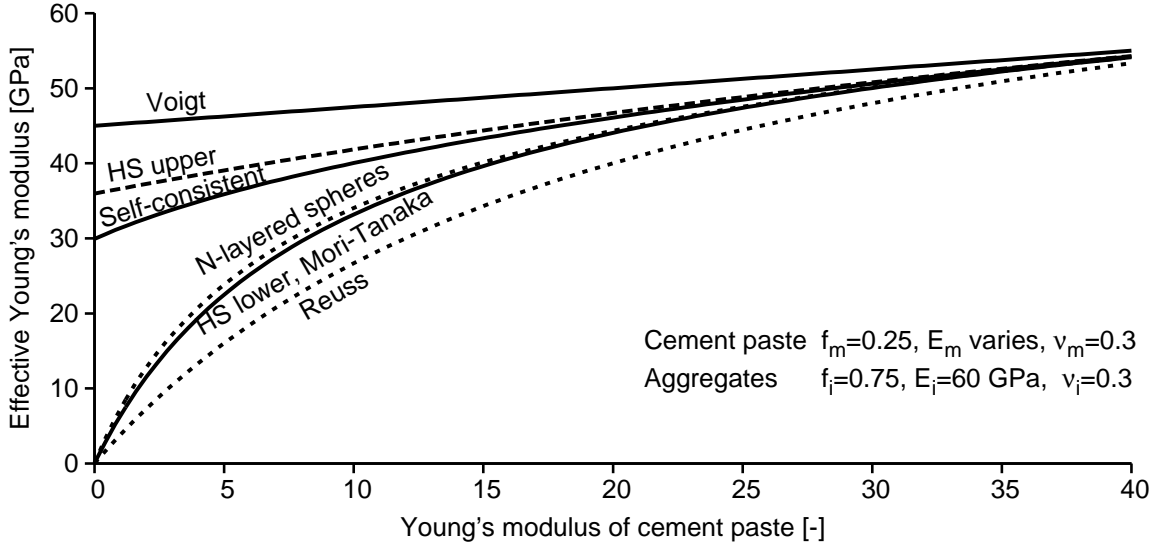


Figure 8: Effective Young's modulus of concrete made from aggregates embedded in a hydrating cement paste.

5.2 Numerical homogenization methods

Generally speaking, numerical methods provide greater flexibility in local constitutive laws, types of boundary conditions, coupled phenomena etc. at the expense of computational time and possible unit cell (UC) discretization. We explore two methods for solving Eqs. (5), (7) with periodic boundary conditions. A local strain tensor is decomposed into the average, or macroscopic part \mathbf{E} , and the fluctuating part $\epsilon^*(\mathbf{x})$

$$\epsilon(\mathbf{x}) = \mathbf{E} + \epsilon^*(\mathbf{x}), \quad (19)$$

The fluctuating strain is first searched via finite element analysis (FEA), leading to

$$\mathbf{K}\mathbf{r} = - \sum_{\text{Elements}} \int_{V_e} \mathbf{B}_e^T \mathbf{D}_e \mathbf{E} dV_e, \quad (20)$$

where \mathbf{K} is the reduced global stiffness matrix, \mathbf{r} is the vector of nodal displacements, \mathbf{B}_e is the strain interpolation matrix of the finite element, \mathbf{D}_e represents a material stiffness matrix

and the vector \mathbf{E} contains prescribed components of the imposed macroscopic strain tensor \mathbf{E} . The vector \mathbf{E} has the same meaning as the eigenstrain (stress-free strain).

The next successive homogenization method is based on the discrete fast Fourier transformation (DFT) [36]. Arbitrary stress field in a composite may be decomposed into the contribution of reference homogeneous material and to the polarization stress:

$$\boldsymbol{\sigma}(\mathbf{x}) = \mathbf{L}(\mathbf{x})\boldsymbol{\epsilon}(\mathbf{x}) = \mathbf{L}^0\boldsymbol{\epsilon}(\mathbf{x}) + \boldsymbol{\tau}(\mathbf{x}), \quad (21)$$

which may be rewritten as iterative procedure:

$$\boldsymbol{\epsilon}^{k+1}(\mathbf{x}) = \mathbf{E} - \int_V \boldsymbol{\Gamma}^0(\mathbf{x} - \mathbf{x}')(\mathbf{L}(\mathbf{x}') - \mathbf{L}^0)\boldsymbol{\epsilon}^k(\mathbf{x}')d\mathbf{x}'. \quad (22)$$

where $\boldsymbol{\Gamma}$ is Green function. The convolution term of Eq. (22) may be efficiently treated by fast Fourier transformation (FFT). Tab. 1 gives the notion of consumed time and memory during homogenization of later stages of cement paste [50].

Size [μm]	DOF's	Memory [MB]		Time [s]	
		FEM	FFT	FEM	FFT
$10 \times 10 \times 10$	2 997	5.7	3.1	1.6	2.6
$25 \times 25 \times 25$	46 872	71.2	6.9	24.3	6.3
$50 \times 50 \times 50$	374 997	503	35.5	218	62
$75 \times 75 \times 75$	1 265 622	1713	109	787	93
$100 \times 100 \times 100$	-	-	256	-	183

Table 1: Approximate computational requirements on CPU 3.2 GHz, FEM - periodic, FFT, uniform mesh.

5.3 Paste of Kamali et al., w/c = 0.5

The paste was hydrated under saturated curing conditions at $\approx 20^\circ\text{C}$ [29]. Fig. 9 shows the evolution of the Young modulus as predicted from the two-level continuum homogenization; C-S- H_{LD} and C-S- H_{HD} are first homogenized using the Mori-Tanaka method and then with the self-consistent scheme at the level of cement paste, Fig. 9. Also, FEM and FFT methods are explored on different sizes of microstructures.

5.4 Analytical approximation of Young's modulus

200 different paste microstructures $50 \times 50 \times 50 \mu\text{m}$ were generated, hydrated by CEMHYD3D model and homogenized by FFT-based method. Analytical approximation in the range of $0.2 \leq$

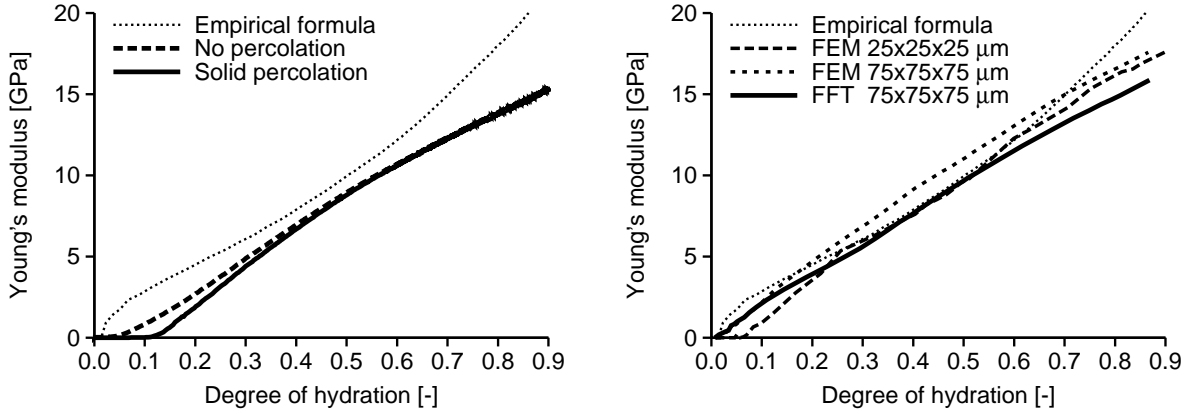


Figure 9: Young's modulus from the two-scale continuum homogenization and numerical homogenization.

$wcr \leq 0.6$ yields

$$\text{Young's modulus [GPa]} = a(\text{DoH} - \text{DoH}_p)^b > 0, \quad (23)$$

$$\text{DoH}_p = 0.1322 wcr - 0.0211, \quad (24)$$

$$a = \frac{1}{0.1256 wcr^{1.346}}, \quad (25)$$

$$b = 2.933 wcr - 0.145, \quad b \leq 1. \quad (26)$$

Fig. 10 displays the evolution of Young's modulus from FFT-based homogenizations and approximations from Equations (23)-(26).

6 Identification of non-aging basic C-S-H creep

This section shows downscaling approach for identification of basic C-S-H creep from the scale of cement paste [52]. For the case of no moisture or temperature change, the flow term in B3 creep model can be simplified to a logarithmic law, which is adopted here. Excluding drying creep, the B3 compliance function for uniaxial stress has the form

$$J(t, t') = \underbrace{q_1}_{\text{elastic}} + \underbrace{C_v(t, t')}_{\text{aging viscoelastic}} + \underbrace{q_4 \ln\left(\frac{t}{t'}\right)}_{\text{flow term}}, \quad (27)$$

$$C_v(t, t') = \int_{t'}^t v^{-1}(t) \dot{C}_g(\tau - t') d\tau = \int_{t'}^t v^{-1}(t) \frac{n(\tau - t')^{n-1}}{\lambda_0^n + (\tau - t')^n} d\tau, \quad (28)$$

$$v^{-1}(t) = \left[q_2 \left(\frac{\lambda_0}{t} \right)^m + q_3 \right]. \quad (29)$$

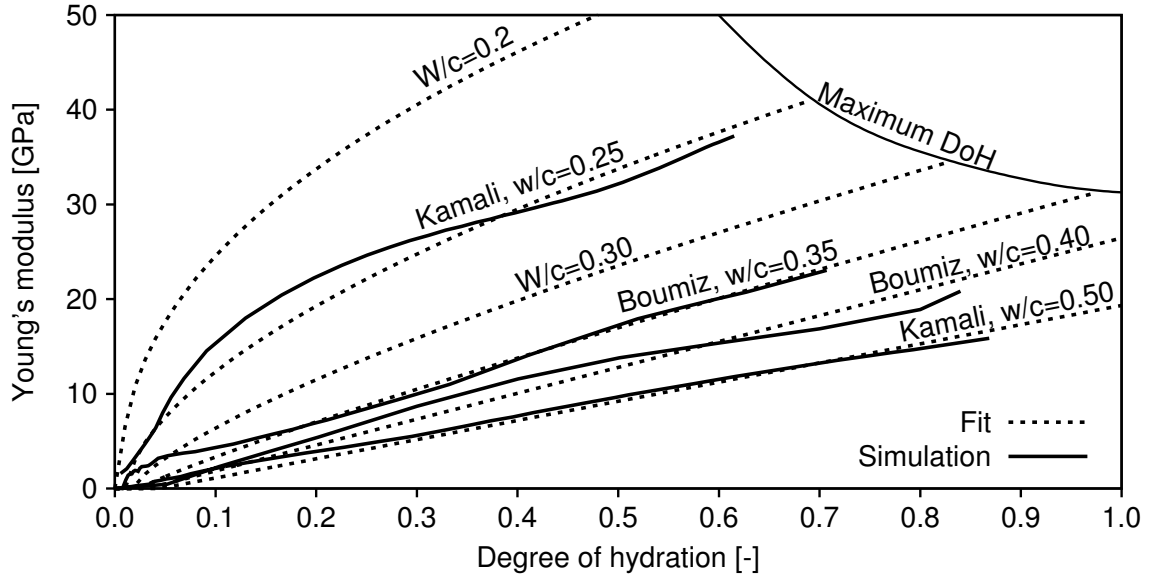


Figure 10: Young's moduli from the FFT homogenization, $75 \times 75 \times 75 \mu\text{m}$, and the fit according to Eq. (23).

Several parameters were found to be constant for concrete, independent of its type and curing conditions: $\lambda_0 \approx 1$ day, $m = 0.5$ and $n = 0.1$ [6].

In an extension of Eq. (27) to stress varying in time, the hypothesis of linearity with respect to stress agrees well with test data under the condition that there is no drying and that the stresses are less than approximately 50 % of the strength limit of concrete, possibly up to 80 % for cement paste [21]. The total strain may thus be calculated according to the principle of superposition, integrating varying strain histories produced by infinitesimal stress increments $\frac{d\sigma(t')}{dt'}$ [3, 4, 28]

$$\epsilon(t) = \int_0^t J(t, t') \frac{d\sigma(t')}{dt'} dt' + \epsilon_0, \quad (30)$$

where ϵ_0 is the initial strain, which includes shrinkage, thermal strain and cracking strain. For a numerical solution, it is convenient to convert Eq. (30) to a rate-type formulation based on the Kelvin or Maxwell chain. For the case of the aging Kelvin chain, see Fig. 11, [3, 28]

$$\dot{\epsilon}_\mu(t) + \tau_\mu \ddot{\epsilon}_\mu(t) = \frac{\dot{\sigma}(t)}{E_\mu(t)}, \quad (31)$$

where τ_μ are properly chosen retardation times of the μ -th Kelvin unit ($\mu = 1, 2, \dots, N$), $E_\mu(t)$ are the corresponding moduli, which in general are age-dependent, and $\epsilon_\mu(t)$ are the strains in individual Kelvin units.

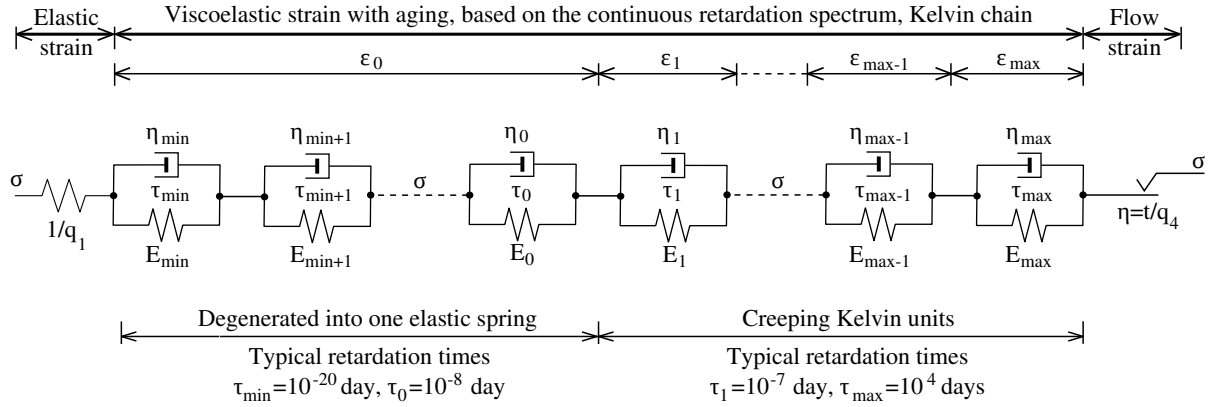


Figure 11: Approximation of aging creep function by non-aging linear spring, aging Kelvin chain and a flow element. The representation corresponds to Eq. (27).

6.1 Visco-elastic homogenization via FFT-based method

The macroscopic viscoelastic response of UC is obtained through the solution of the local problem, which consists of equilibrium and constitutive equations complemented by boundary conditions. According to the exponential algorithm [2], two equations must be satisfied in each time step

$$\operatorname{div} \Delta \boldsymbol{\sigma}(\boldsymbol{x}) = 0, \quad (32)$$

$$\Delta \boldsymbol{\sigma}(\boldsymbol{x}) = \mathbf{L}''(\boldsymbol{x}) : (\Delta \boldsymbol{\epsilon}(\boldsymbol{x}) - \Delta \boldsymbol{\epsilon}''(\boldsymbol{x})) = \mathbf{L}''(\boldsymbol{x}) : \Delta \boldsymbol{\epsilon}(\boldsymbol{x}) - \Delta \boldsymbol{\lambda}(\boldsymbol{x}), \quad (33)$$

where the inelastic strain increment $\Delta \boldsymbol{\epsilon}''(\boldsymbol{x})$ is known from a previous time step and can be replaced, after the multiplication with the incremental stiffness tensor, by the eigenstress tensor $\Delta \boldsymbol{\lambda}(\boldsymbol{x})$. The periodic boundary conditions are expressed as a decomposition of strain increments into the average $\Delta \boldsymbol{E}$ and the fluctuating part $\Delta \boldsymbol{\epsilon}^*(\boldsymbol{x})$

$$\Delta \boldsymbol{\epsilon}(\boldsymbol{x}) = \Delta \boldsymbol{E} + \Delta \boldsymbol{\epsilon}^*(\boldsymbol{x}). \quad (34)$$

which yields

$$\begin{aligned} \Delta \boldsymbol{\epsilon}(\boldsymbol{x}) &= \Delta \boldsymbol{E} - \boldsymbol{\Gamma}^0(\boldsymbol{x}) * \Delta \boldsymbol{\tau}(\boldsymbol{x}) = \\ &= \underbrace{\Delta \boldsymbol{E} + \boldsymbol{\Gamma}^0(\boldsymbol{x}) * (\mathbf{L}^0 : \Delta \boldsymbol{\epsilon}(\boldsymbol{x}))}_{\Delta \boldsymbol{\epsilon}(\boldsymbol{x})} - \boldsymbol{\Gamma}^0(\boldsymbol{x}) * \underbrace{(\mathbf{L}''(\boldsymbol{x}) : \Delta \boldsymbol{\epsilon}(\boldsymbol{x}) - \Delta \boldsymbol{\lambda}(\boldsymbol{x}))}_{\Delta \boldsymbol{\sigma}(\boldsymbol{x}) \text{ from Eq. (33)}}. \end{aligned} \quad (35)$$

This equation is the basis of a recursive iterative procedure ($k = 0, 1 \dots$) for viscoelasticity

$$\Delta \boldsymbol{\epsilon}^{k+1}(\boldsymbol{x}) = \Delta \boldsymbol{\epsilon}^k(\boldsymbol{x}) - \boldsymbol{\Gamma}^0(\boldsymbol{x}) * \Delta \boldsymbol{\sigma}^k(\boldsymbol{x}). \quad (36)$$

The local constitutive law in Eq. (33) has to be called in each iteration to access $\Delta \boldsymbol{\sigma}^k(\boldsymbol{x})$.

6.2 Inverse creep analysis for two-year old cement paste

The irreversible creep of C-S-H will be obtained from the unloading stage of hardened cement paste two years old, with a $w_{cr} = 0.5$ [7]. Pairs of T-shaped bars were cut from the stored cylinders, Fig. 12, and subjected to an axially compressive load of 10.35 MPa in a humidity-controlled chamber, which was maintained at 96 % RH instead of 100 % due to technical difficulties. After 72 hours, the specimens were unloaded. Drying shrinkage was measured on a companion load-free specimen.

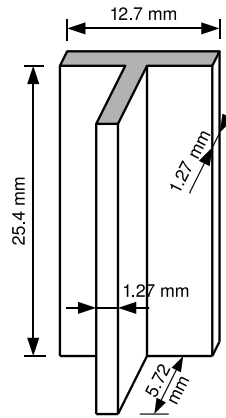


Figure 12: T-shaped bar used in creep and shrinkage tests of cement pastes [58].

Two UCs $10 \times 10 \times 10$ and $50 \times 50 \times 50 \mu\text{m}$ of cement paste were reconstructed using the CEMHYD3D model. The larger UC truncates cement particles above $19 \mu\text{m}$ in diameter and the smaller UC those above $5 \mu\text{m}$. Fig. 13 shows both at the time of two years. The chemical composition of clinker was normalized according to the aforementioned data, and the cement particle size distribution was taken to be the same as for reference cement 16132 with the Blaine fineness of $357 \text{ m}^2/\text{kg}$ and autocorrelation files from reference cement 115 of the NIST database, see [10]. Hydration with the CEMHYD3D code reached the degree of hydration of 0.988, for which the important volume fractions were: calcium hydroxide 0.141, C-S- H_{LD} 0.303, C-S- H_{HD} 0.183, unhydrated clinker mineral 0.004, water-filled capillary porosity 0.199, and empty capillary porosity 0.003 caused by the inaccessibility of certain parts of UC to pore water even at saturated curing conditions. The C-S- $H_{HD}/(\text{C-S-}H_{HD} + \text{C-S-}H_{LD})$ ratio was 0.376, which agrees well with the colloid model [60].

The T-shaped specimens were simultaneously in the process of drying to 96 % RH and loading. The measured shrinkage strain [8] was fitted as [5]

$$\epsilon_{sh}(t) = 0.165 \tanh \sqrt{\frac{(t - t') - 0.1}{\tau_{sh}}}, \quad (t - t') \geq 0.1 \text{ day}, \quad (37)$$

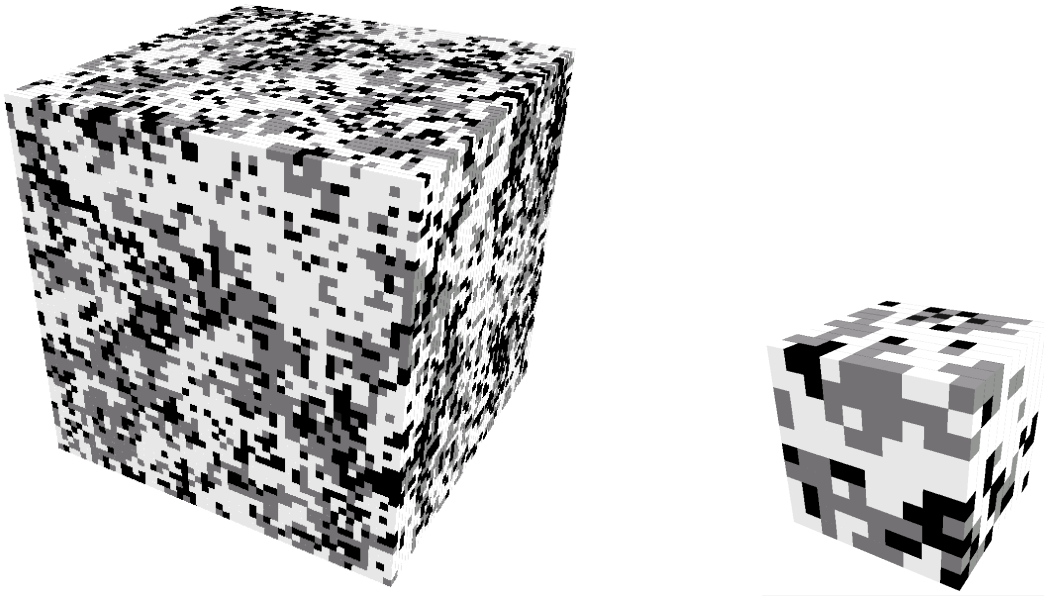


Figure 13: UC of cement paste $50 \times 50 \times 50 \mu\text{m}$ (left) and $10 \times 10 \times 10 \mu\text{m}$ (right). White = C-S-H (viscoelastic), gray = other solids (elastic), black = capillary porosity.

where 0.1 day is the time at which drying began to have an effect on the specimen, and $\tau_{sh} = 0.8$ day is the shrinkage half-time, Fig. 14. The uncertainties in Eq. (37) have only a small effect on the irrecoverable strain after unloading. It is further assumed that shrinkage and creep strain are additive for these nearly saturated conditions.

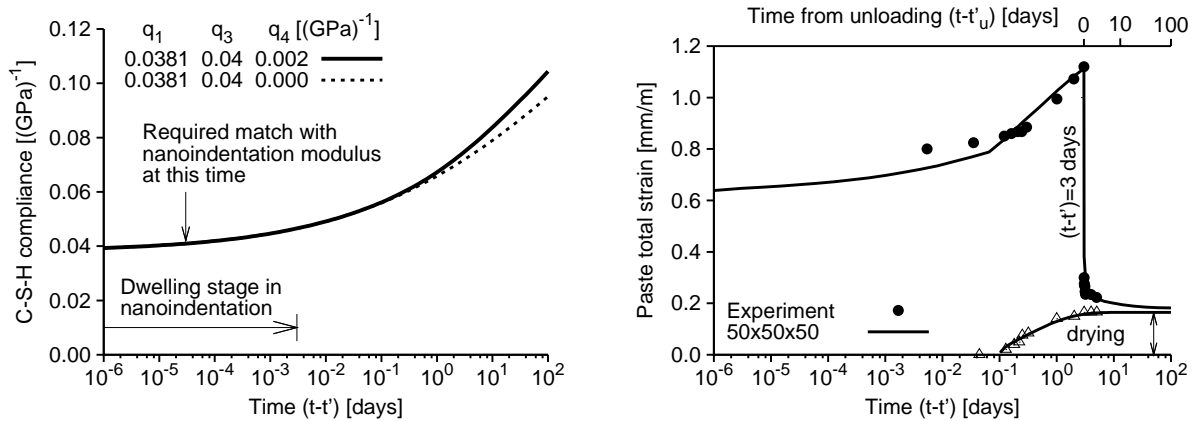


Figure 14: Compliance assigned to C-S-H (left), also for comparison without the flow term ($q_4 = 0$). Measured and simulated total strain of two-year old cement paste (right). The arrows show corresponding times from nanoindentation experiments.

The parameters q_1 , q_3 , q_4 , λ_0 , n for the C-S-H creeping phase in the B3 model remain unknown. The parameter q_4 quantifies the irrecoverable flow strain which can be determined from unloading, independently of the other parameters of mature paste. The parameters q_1 and q_3 are in fact related through nanoindentation data. The results are summarized in Tab. 2.

Experiment	Two-year old paste
q_1 [(GPa) ⁻¹]	0.0381
q_2 [(GPa) ⁻¹]	0.0
q_3 [(GPa) ⁻¹]	0.040
q_4 [(GPa) ⁻¹]	0.002
m [-]	no effect
n [-]	0.25
λ_0 [day]	1
$1/J(t + 2.6 \text{ s}, t)$ C-S-H [GPa] ^b	24.31
Poisson's ratio of C-S-H [-]	0.24
t' [day] ^c	1
Kelvin units	11
τ_1 [day]	10^{-7}
τ_{max} [day]	10^3
Max. attained iterations	300

^b approximately corresponding to Young's modulus from nanoindentation data

^c due to non-aging creep takes effect only in the microprestress (flow) term

Table 2: Assigned C-S-H parameters and homogenization details in the analysis of non-aging two-year and 30-year old cement pastes.

Fig. 14 shows viscoelastic behavior assigned to C-S-H, both with and without the flow term ($q_4 = 0$). An arrow points to the time when the elastic indentation modulus is typically evaluated. The asymptotic compliance $q_1 = 0.0381 \text{ GPa}^{-1}$ is about 93 % of the compliance from nanoindentation data $J(t + 3 \cdot 10^{-5} \text{ day}, t) = 0.0411 \text{ GPa}^{-1}$. Also, the time range for the creep nanoindentation test is displayed for a typical duration of 4.3 minutes. The elastic strain immediately after loading was not directly reported [7] and was assumed to be $800 \cdot 10^{-6}$ for a static stress of 10.35 MPa at 0.01 day, see Fig. 14.

6.3 Long-term creep upscaled to the concrete level

Upscaling of creep through the correspondence principle is possible as long as the compliance function takes the form $J(t - t')$. The creep function with aging generally has the form $J(t, t')$, see Eq. (27) for the B3 model. To circumvent this difficulty, Grasley and Lange [20] used, among others, the time-shift approach where the creep function is expressed in the form $J(\xi(t) - \xi(t'))$. The function $\xi(t)$ maps real time to pseudotime. Pichler and Lackner [42] made the compliance function $J(t - t')$ dependent also on DoH so the homogenized creep depends

also on t' .

Let us try to approximate the basic creep of concrete with the non-aging version of the B3 model. Brooks [13] performed unique basic creep tests under a constant uniaxial loading for the duration of 30 years. He found that the reversible part, evaluated at six months after unloading, is only 5 – 14 %. The irreversible viscoelastic part of the B3 model originate either from the aging or from the flow term, see Eq. (27). The flow term can be approximated in the form $J(t - t')$ under the condition that stress in the C-S-H phase decays rapidly with time

$$q_4 \ln \left(\frac{t}{t'} \right) = q_4 \ln \left(1 + \frac{t - t'}{t'} \right) \approx q_4 \ln \left(1 + \frac{t - t'}{1} \right). \quad (38)$$

Fig. 15 shows such a creep compliance at four different scales. The considered concrete with a $wcr = 0.5$ is made from a normal weight aggregate quarried in North Notts. The parameters for B3 models were taken from Tab. 2; $q_1 = 0.0381$, $q_2 = 0$, $q_3 = 0.040 \text{ (GPa)}^{-1}$, $n = 0.25$, $m = 0.5$ and q_4 was fitted to 0.017 (GPa)^{-1} . Young's modulus of coarse and fine aggregates was assumed as 60 GPa, Poisson's ratio as 0.2. The air present in concrete was considered to act simultaneously at the level of cement paste. The Mori-Tanaka method was used for the transition among all three scales and no ITZ was considered.

7 Multiscale simulation of heat transport

The temperature rise in hydrating concrete presents a formidable problem which may lead to a significant acceleration of hydration kinetics, early age cracking, or decreased durability. Low thermal conductivity of concrete, the exothermic hydration process and surrounding ambient conditions contribute to temperature gradients, often accompanied with strains. Tensile stresses then appear in a cooling stage due to minor restraints and excessive stresses may lead to the formation of microcracks manifested with decreased durability [39, 47]. Several guidelines require that temperature anywhere in concrete should not exceed 70°C to avoid a possible risk of delayed ettringite formation accompanied by expansion and disintegration [1]. Other rules specify a maximum cooling rate of 3°C per hour during the first 24 hours and special caution when the concrete temperature drops below 4°C [37].

7.1 Mathematical formulation of heat transport

The transient three dimensional heat conduction problem in incompressible media can be derived from energy balance on a differential element [33, 62]

$$-\nabla^T \mathbf{q}(\mathbf{x}) + \bar{Q}(\mathbf{x}, t) = \rho(\mathbf{x})c_V(\mathbf{x}) \frac{\partial T(\mathbf{x}, t)}{\partial t}, \quad (39)$$

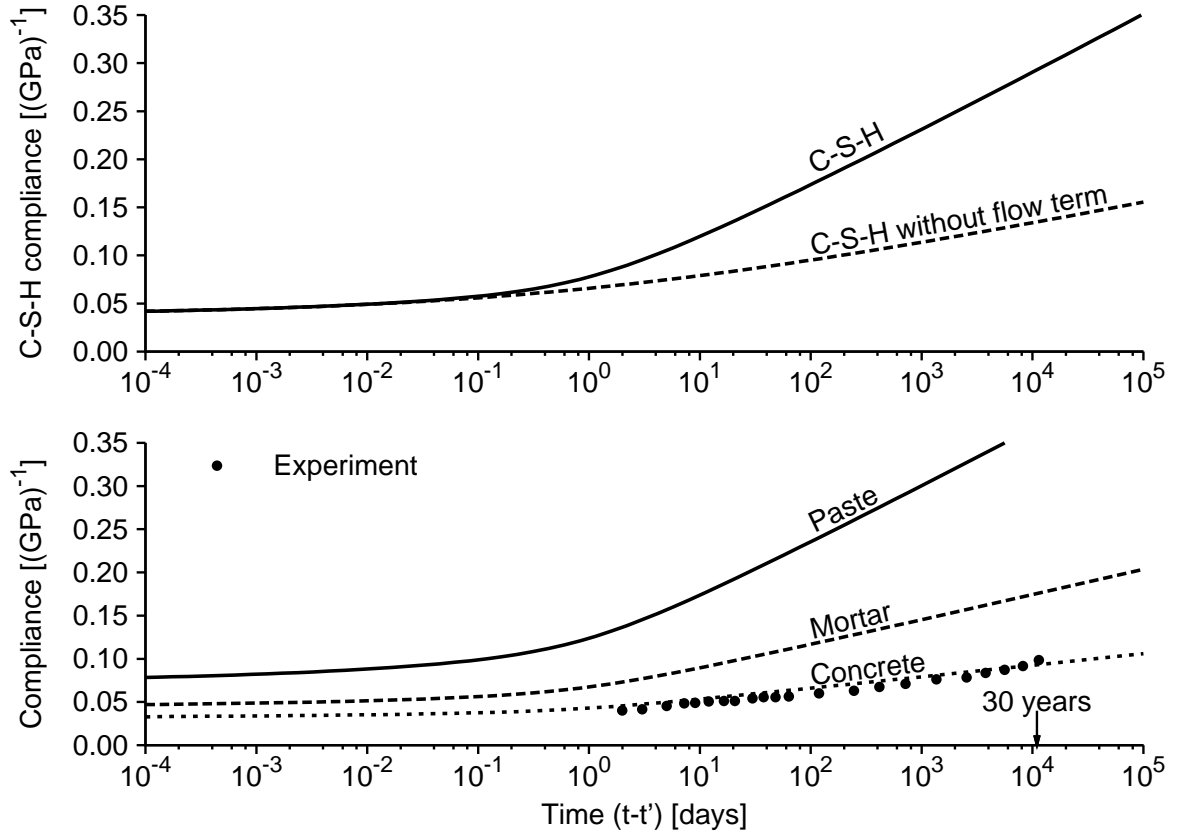


Figure 15: Creep at four scales as predicted by continuum homogenization methods, $w_{cr} = 0.5$.

where $\mathbf{q}(\mathbf{x})$ [W/m^2] is the heat flux originating from heat conduction, $\bar{Q}(\mathbf{x}, t)$ [W/m^3] represents a known heat source from the scale of cement paste, $\rho(\mathbf{x})$ [kg/m^3] stands for concrete density, $c_V(\mathbf{x})$ [$\text{Jkg}^{-1}\text{K}^{-1}$] is a specific heat capacity and $T(\mathbf{x}, t)$ [K] represents the unknown temperature field. The derivation further considers an isotropic material. $\bar{Q}(\mathbf{x}, t)$ is obtained from hydration models, see Section 4.

The heat flux over the body, $\mathbf{q}(\mathbf{x})$, corresponds to heat conduction, which is expressed by Fourier's law

$$\mathbf{q}(\mathbf{x}) = -\lambda(\mathbf{x})\nabla T(\mathbf{x}), \quad (40)$$

where $\lambda(\mathbf{x})$ [$\text{Wm}^{-1}\text{K}^{-1}$] is the thermal conductivity of an isotropic material.

The solution of Eq. (39) requires prescribing initial conditions $\bar{T}(\mathbf{x}, 0)$ at $t = 0$ over the body

$$T(\mathbf{x}, 0) = \bar{T}(\mathbf{x}, 0), \quad \mathbf{x} \in \Omega. \quad (41)$$

The differential Eq. (39) can be complemented with boundary conditions, which have a

variety of forms. Dirichlet's boundary condition prescribes temperature on the boundary

$$T(\mathbf{x}, t) = \bar{T}(\mathbf{x}, t), \quad \mathbf{x} \in \Gamma_T. \quad (42)$$

Neumann's boundary condition prescribes the flux $\bar{q}(\mathbf{x}, t)$ on the boundary

$$\mathbf{n}(\mathbf{x})^T \mathbf{q}(\mathbf{x}, t) = \bar{q}(\mathbf{x}, t), \quad \mathbf{x} \in \Gamma_{\bar{q}}, \quad (43)$$

where $\mathbf{n}(\mathbf{x})$ is a unit normal vector pointing outwards from the surface.

Cauchy's (mixed) boundary condition can be represented by heat convection. Let us consider a concrete surface exposed to air. The air flows around the concrete body and forms a thin region called the boundary layer. Convection occurs inside the layer and sweeps the heat from the concrete surface. The heat flux is described by Newton's law on the body surface

$$\mathbf{n}(\mathbf{x})^T \mathbf{q}(\mathbf{x}) = h(\mathbf{x}) (T(\mathbf{x}) - T_\infty), \quad \mathbf{x} \in \Gamma_c, \quad (44)$$

where $h(\mathbf{x})$ [$\text{Wm}^{-2}\text{K}^{-1}$] is a heat transfer coefficient and T_∞ is the ambient temperature far enough from the boundary layer.

7.2 Space and time discretization

The analytical solution of Eq. (39) is not amenable for more complicated cases. FEM presents a robust numerical procedure, which starts from the formulation of a weak problem. This yields a set of linear set of algebraic equations in the form

$$\mathbf{C}\dot{\mathbf{r}} + \mathbf{K}\mathbf{r} = \mathbf{p}, \quad (45)$$

where $\dot{\mathbf{r}}$ are temperature nodal derivatives with respect to time. The system matrices and the heat load vector are provided by

$$\mathbf{K} = \int_{\Omega} \mathbf{B}(\mathbf{x})^T \lambda(\mathbf{x}) \mathbf{B}(\mathbf{x}) d\Omega, \quad (46)$$

$$\mathbf{C} = \int_{\Omega} \mathbf{N}(\mathbf{x})^T \rho(\mathbf{x}) c_V(\mathbf{x}) \mathbf{N}(\mathbf{x}) d\Omega, \quad (47)$$

$$\mathbf{p} = - \int_{\Gamma_{c, T, \bar{q}}} \mathbf{N}(\mathbf{x})^T \mathbf{n}(\mathbf{x})^T \mathbf{q}(\mathbf{x}, t) d\Gamma + \int_{\Omega} \mathbf{N}(\mathbf{x})^T \bar{Q}(\mathbf{x}, t) d\Omega, \quad (48)$$

where \mathbf{K} is the conductivity matrix, \mathbf{C} is the capacity matrix, and the heat load vector, \mathbf{p} , captures both the boundary conditions and the heat source. All terms depending on temperature will appear on the left hand side of Eq. (45).

Now assume that Eq. (45) is evaluated at a time step t_{n+1} using a parameter $\alpha \in \langle 0, 1 \rangle$ so that $t = t_n + \alpha \Delta t_n$. Inserting such approximation into Eq. (45) yields

$$(\mathbf{C} + \alpha \Delta t \mathbf{K}) \dot{\mathbf{r}}_{n+1} = \mathbf{p}_{n+1} - \mathbf{K} \tilde{\mathbf{r}}_{n+1}, \quad (49)$$

which will provide an unknown temperature derivative $\dot{\mathbf{r}}_{n+1}$. A back-substitution gives the unknown vector \mathbf{r}_{n+1}

$$\mathbf{r}_{n+1} = \tilde{\mathbf{r}}_{n+1} + \alpha \Delta t_n \dot{\mathbf{r}}_{n+1}. \quad (50)$$

7.3 Validation

Multiscale heat transport model with validations was published previously [27, 49, 50, 51, 56]. This section provides a brief overview.

7.3.1 Temperature evolution on a prestressed bridge

A new scaffold bridge “Nové spojení” was erected during 2006-2007 in Prague, see the photo in Fig. 16. The prestressed bridge, totaling 443 m in length, acts as a continuous beam with 12 spans. The temperature field was gathered at many gauges up to several days after the concrete casting. Fig. 17 shows a characteristic cross-section of the bridge and the sequence of construction steps, which followed an enumerated, bottom-top approach:

1. Placing precast segments made of face concrete,
2. Casting the bottom slab with a thickness of 363–850 mm,
3. Casting two beams with a height of approximately 2.0 m and a minimum width of 1.3 m, joined by a massive cross-beam above the piers, see Fig. 16,
4. Placing the precast segments below the top slab, creating a sacrificial formwork,
5. Casting the top slab with a variable thickness.

The simulation deals with hydration of the bridge beams. This had occurred after 35 days from the slab casting, from 6:39 AM, Jul 12, 2006. Fig. 18 shows the beam dimensions and a generated mesh with 239 nodes, 39 triangular and 177 quadrilateral elements, totaling 239 DoFs. The simulation utilizes horizontal bridge symmetry. Gauge T5 in Fig. 18 was considered to be the most important from the underlying slab. The mesh was adjusted in such a way that gauges T5 – T10 were forced to be at the nodal positions. Again, the beam was separated into five regions and five hydration models were assigned to them, see Fig. 18.

According to the measured data, the simulation considered the initial ambient temperature of 26°C and 25°C for concrete. The time functions of ambient air temperature were approximated



Figure 16: Construction of the scaffold bridge in Prague, photo by D. Prause.

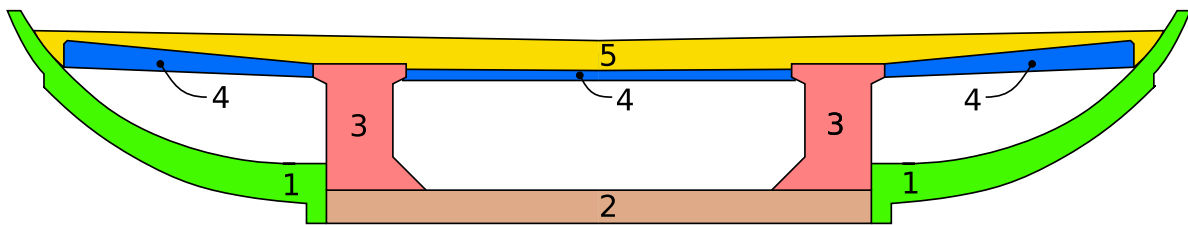


Figure 17: A characteristic cross-section of the bridge and a sequence of construction steps.

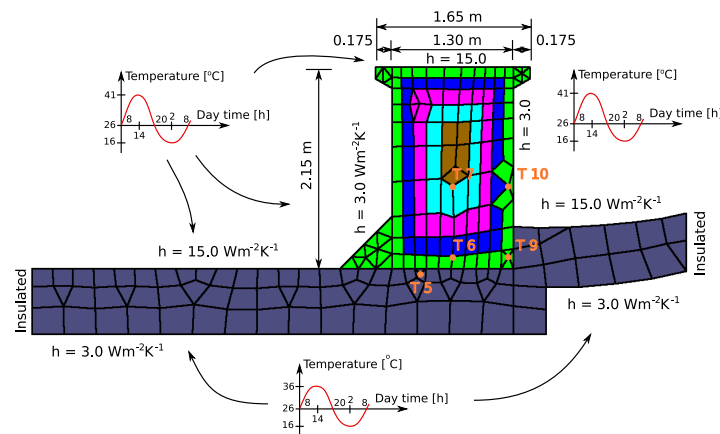


Figure 18: Topology and boundary conditions of the beam. Different colors represent different CEMHYD3D material models, the right shoulder and the bottom slab are considered mature.

at the bottom as

$$T(t) = 26 + 10 \sin \left\{ 2\pi t - \frac{2.7\pi}{24} \right\}, \quad (51)$$

and at the top and the vertical surfaces as

$$T(t) = 26 + \left[10 + 5 \cdot H \left(\sin \left\{ 2\pi t - \frac{2.7\pi}{24} \right\} \right) \right] \cdot \sin \left\{ 2\pi t - \frac{2.7\pi}{24} \right\}. \quad (52)$$

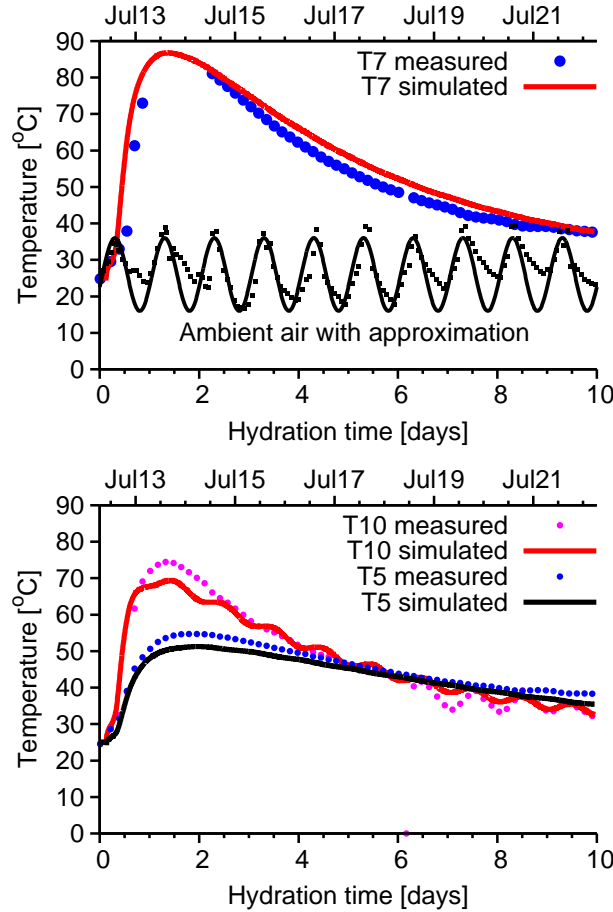
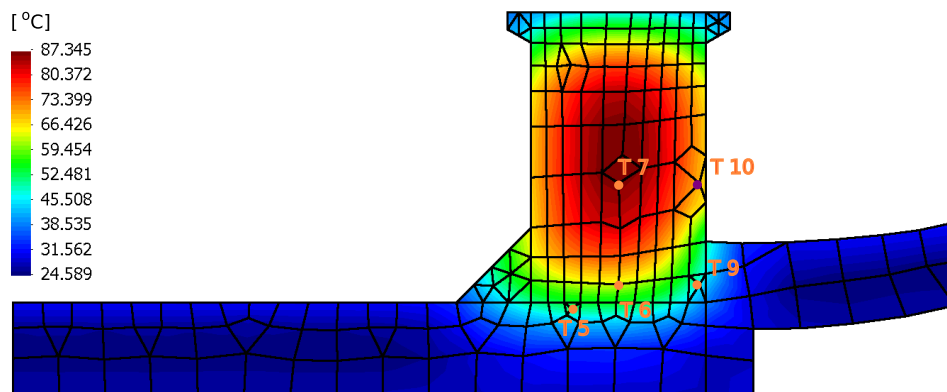


Figure 19: Temperature of gauges T7, T10, T5 and approximated ambient temperature.

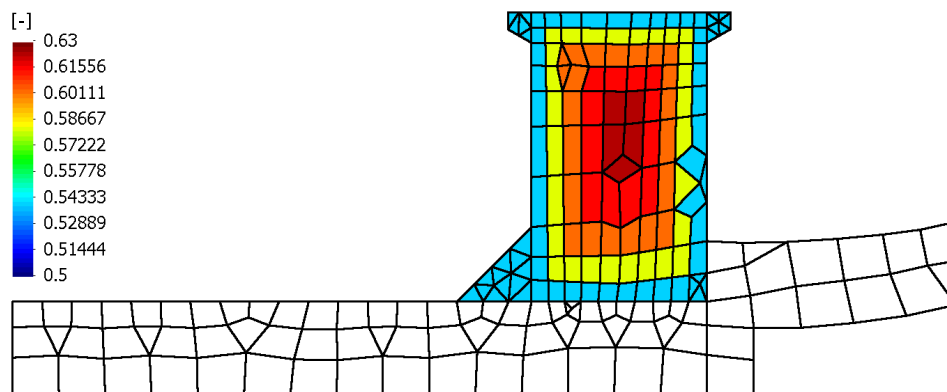
Pair gauges T5–T6 and T9–T10 measured very similar temperature values. For this reason, only gauges T7, T10, and T5 were validated, see Fig. 19. The maximum temperature in gauge T7 was not measured due to technical difficulties but the simulation predicted 86.8°C at 1.367 day, for the cement amount of 400 kg/m^3 . The approximation of ambient air temperature is in reasonable agreement with the sinusoidal function described by Eq. (51).

Fig. 20 displays details for the maximum temperature of 86.8°C in gauge T7, achieved at 1.367 day. Note a low temperature gradient in the middle part of the beam, which approaches adiabatic conditions. The variation in DoH and Young's modulus of concrete is not significant during this hydrating stage. The whole beam simulation took 68 minutes on the 3.2 GHz PC and occupied 19 MB of RAM excluding homogenization routines. Calculations covered 10 days of

Temperature field



Degree of hydration



Young's modulus of concrete

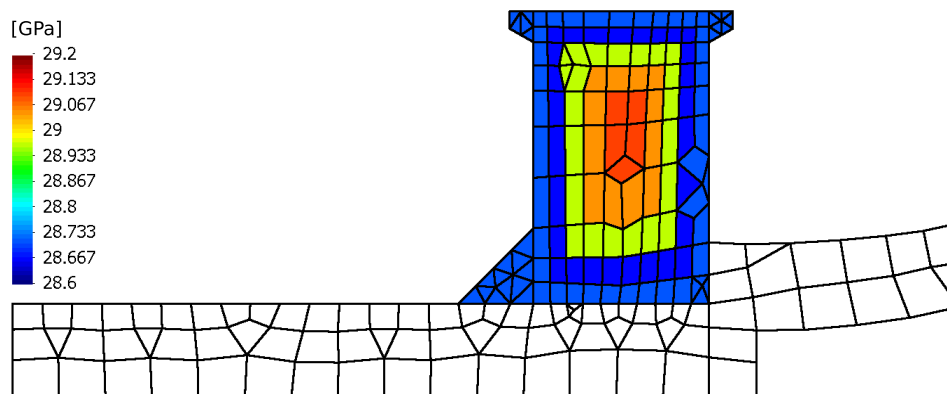


Figure 20: Temperature field, DoH and Young's modulus of concrete at 1.367 day when maximum temperature 86.8 $^{\circ}\text{C}$ is reached in gauge T7.

the hydration period with the time integration step of 10 minutes using the Crank-Nicolson scheme.

7.3.2 Optimal position of cooling pipes

This example demonstrates how multiscale modeling can be applied for the optimization of the cooling pipes positions. The pipes were embedded in massive concrete and circulating water efficiently dissipates the hydration heat.

The field data came from the construction of the Oparno bridge arch in the Czech Republic, which spans 135 m, see Fig. 21. Fig. 22 shows a symmetrical left part of an arch cross-section. The cross-section in the form of a π -shape has the outer dimensions of 7.0×2.4 m. The inner part corresponds well to adiabatic curing conditions. The arch is cast incrementally in segments during the whole year.



Figure 21: The Oparno bridge, Czech Republic, 2010.

The simulation will explore the worst scenario during the summer casting. The initial concrete temperature is set at 23°C and the surrounding ambient temperature at 30°C . The contractor prescribed the mix composition hence all optimization has to deal with boundary conditions. In the absence of cooling, the maximum concrete temperature attains 95°C at 52 hours after casting, which was unacceptable, see Fig. 22-a.

The original cooling, captured in Fig. 22-b, proved to be effective in the decrease of the maximum temperature to 69.5°C , but the distribution of temperature is inappropriate. The cooling would induce high tensile stresses at the surface regions, which may lead to cracking with decreased durability. By a judgment, the mutual distance of the cooling pipes was increased so that the temperature was distributed more uniformly, Fig. 22-c. The maximum temperature reached 75°C . When cooling water is switched off after 52 hours of hydration, a hot core forms in the concrete, Fig. 22-d. The field resembles a feasible temperature distribution from Fig. 22-a, but now with lower temperatures.

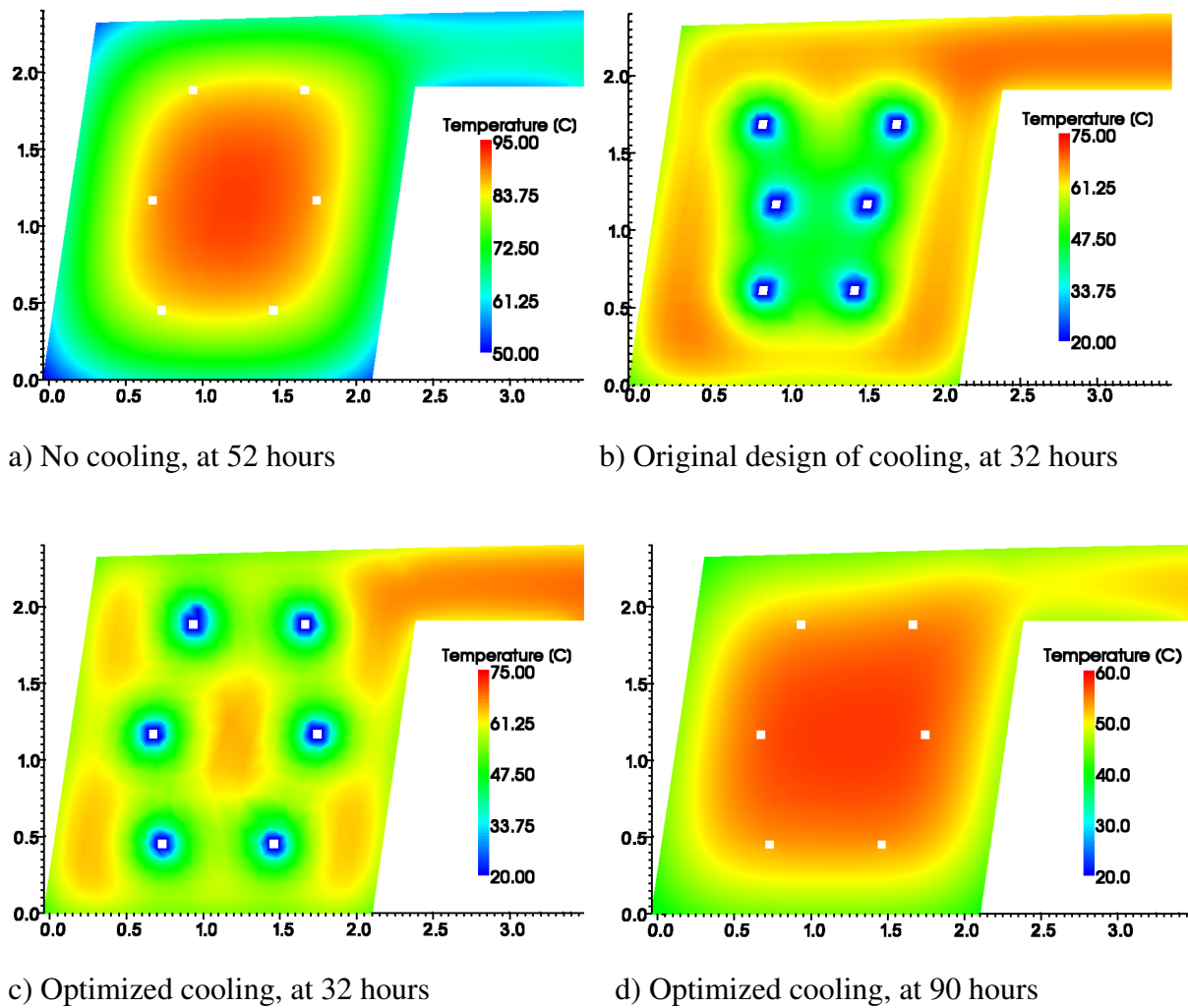


Figure 22: Temperature distribution during concrete casting in summer. Subfigures show important stages during the optimization of cooling pipes with the time corresponding to the highest achieved temperature.

At the end, optimized design of cooling pipes according to Fig. 22-c was used. Temperature gauges recorded values in the arch center and surrounding ambient air. This provided necessary information for an update of model parameters such as initial concrete temperature and hydration kinetics. Fig. 23 shows differences between the blind prediction and updated simulation. Considering number of parameters entering the computation, the differences are acceptable and demonstrate good potential of multiscale methods.

7.3.3 Further validations for concrete temperatures

The multiscale method for temperature prediction is the basis of software ConTemp – A virtual thermo-mechanical simulator for hydrating reinforced concrete blocks [51]. We have been developing this software since 2012 and it is now used in approximately 20 countries in the world

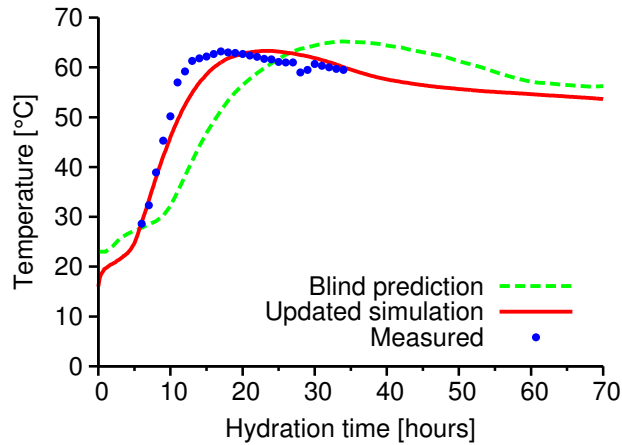


Figure 23: Temperature evolution in the center of the Oparno bridge arch. Results from blind prediction and updated simulation.

by LafargeHolcim company.

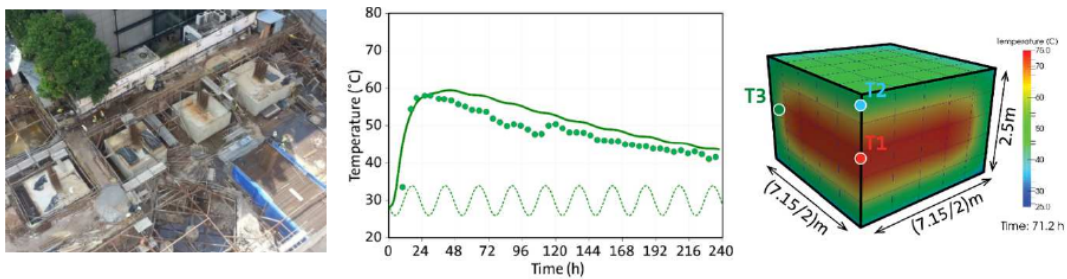


Figure 24: Pile cap foundations in Access Tower II $7.15 \times 7.15 \times 2.5$ m, Sri Lanka, 2014-2016.

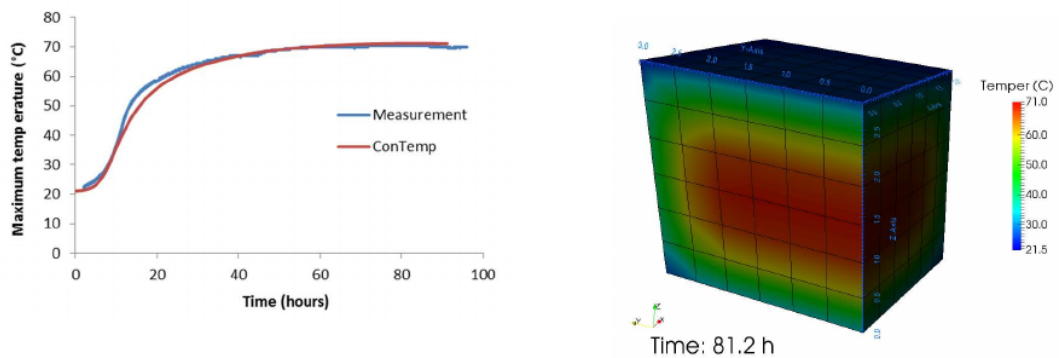
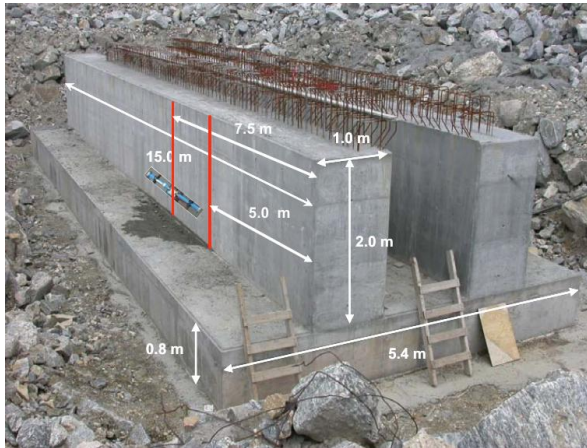
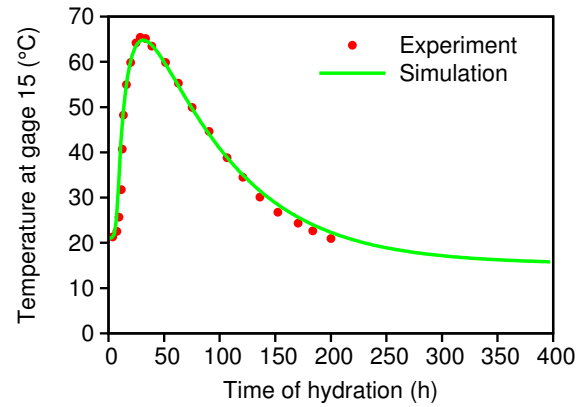


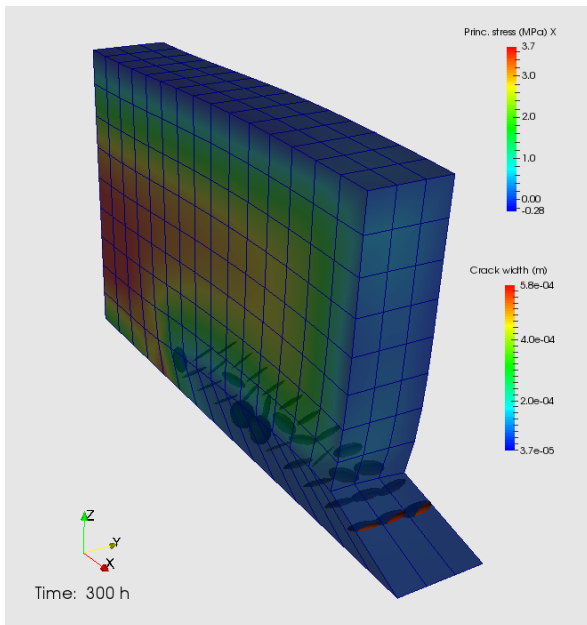
Figure 25: Gas turbine foundation in Ecuador $20 \times 6 \times 2.8$ m, 2014. Only block $3 \times 3 \times 2.8$ m is simulated.



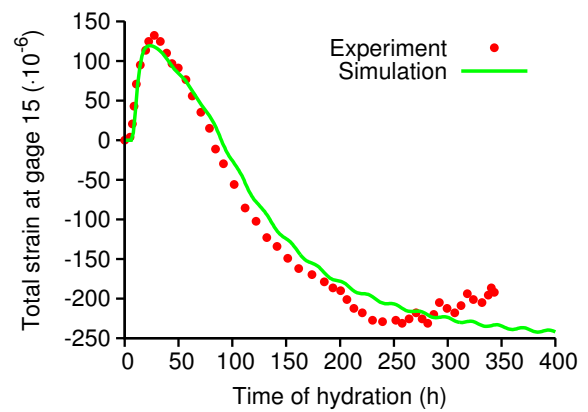
a) Overview



b) Temperature evolution



c) Stress and cracking



d) Strain

Figure 26: Simulation of a restrained wall in Oslo. Gauge 15 is located 1.2 from the bottom in the middle of the wall.

8 Conclusions

Hierarchical modeling presents a powerful framework for assessing nonlocalized phenomena, such as elasticity, viscoelasticity and hydration heat of cement-based materials. These topics were widely discussed, demonstrated and validated employing microstructural models of hydrating Portland-cement paste. ConTemp software emerged from those models, adopted by the largest cement manufacturer LafargeHolcim.

Extension to localized phenomena, such as evolution of compressive strength of blended cement pastes, has been proposed and successfully validated [25, 61]. Base on those experiments, cantilever beams 20 μm long were tested in fruitful collaboration with the Czech Academy of Sciences yielding new information on tensile properties on microscale [40]. Further experimental and numerical campaigns execute in these days to explore the role of interfaces, internal defects and binding properties of N-A-S-H gels. Multiscale insight provides a nice framework for describing these phenomena.

9 Acknowledgement

Many researchers should be acknowledged for their contribution. Particularly Z. Bittnar, J. Zeman, J. Němeček, M. Lepš, J. Kruis, P. Kabele, B. Patzák, M. Jirásek, L. Kopecký, M. Vokáč, R. Chamrová (EPFL), K. Scrivener (EPFL), and Z.P. Bažant (Northwestern University). Former Ph.D. students contributed as well, particularly P. Hlaváček, and M. Hlobil. D.P. Bentz and E.J. Garboczi are acknowledged for their work on the CEMHYD3D hydration model and for their kindness in releasing the model. T. Matschei and L. Baquerizo acted as industrial representatives of Holcim, Lafarge and LafargeHolcim companies and were at the origin of ConTemp modeling tool.

10 References

- [1] R. Barbarulo, H. Peycelon, S. Prené, and J. Marchand. Delayed ettringite formation symptoms on mortars induced by high temperature due to cement heat of hydration or late thermal cycle. *Cem. Concr. Res.*, 35(1):125–131, 2005.
- [2] Z. P. Bažant. Numerically stable algorithm with increasing time steps for integral-type aging creep. In T. Jaeger, editor, *Proc. of 1st Int. Conf. on Struct. Mech. in Reactor Tech. (SMiRT-1)*, pages 119–126, 1971.

-
- [3] Z. P. Bažant. *Creep and Shrinkage in Concrete Structures*. J. Wiley & Sons, London, 1982. Chapter 7. Mathematical models for creep and shrinkage of concrete.
- [4] Z. P. Bažant. *Mathematical Modeling of Creep and Shrinkage of Concrete*. J. Wiley, Chichester and New York, 1988. State of the art in mathematical modeling of creep and shrinkage of concrete.
- [5] Z. P. Bažant and S. Baweja. Creep and shrinkage prediction model for analysis and design of concrete structures: Model B3. Technical report, Am. Concrete Institute, 2000.
- [6] Z. P. Bažant and S. Prasannan. Solidification theory for concrete creep: I. Formulation. *J. Engng. Mech.*, 115(8):1691–1703, 1989.
- [7] J. J. Beaudoin and B. T. Tamtsia. Creep of Hardened Cement Paste - The Role of Interfacial Phenomena. *Interface Science*, 12:353–360, 2004.
- [8] J. J. Beaudoin and B. T. Tamtsia. Effect of Drying Methods on Microstructural Changes in Hardened Cement Paste: an A.C. Impedance Spectroscopy Evaluation. *Journal of Advanced Concrete Technology*, 2(1):113–120, 2004.
- [9] D. P. Bentz. CEMHYD3D: A Three-Dimensional Cement Hydration and Microstructure Development Modeling Package. Version 2.0. Technical report, NIST Building and Fire Research Laboratory, Gaithersburg, Maryland, 2000.
- [10] D. P. Bentz. CEMHYD3D: A Three-Dimensional Cement Hydration and Microstructure Development Modeling Package. Version 3.0. Technical report, NIST Building and Fire Research Laboratory, Gaithersburg, Maryland, 2005.
- [11] O. Bernard, F.-J. Ulm, and T. Germaine. Volume and deviator creep of calcium-leached cement-based materials. *Cem. Concr. Res.*, 33(8):1127–1136, 2003.
- [12] O. Bernard, F.-J. Ulm, and E. Lemarchand. A multiscale micromechanics-hydration model for the early-age elastic properties of cement-based materials. *Cem. Concr. Res.*, 33(9):1293–1309, 2003.
- [13] J. J. Brooks. 30-year creep and shrinkage of concrete. *Magazine of Concrete Research*, 57(9):545–556, 2005.
- [14] M. Cervera, J. Oliver, and T. Prato. Thermo-chemo-mechanical model for concrete. I: Hydration and aging. *Journal of Engineering Mechanics ASCE*, 125(9):1018–1027, 1999.

-
- [15] J. D. Eshelby. The determination of the elastic field of an ellipsoidal inclusion and related problems. In *Proc. Royal Society of London A*, pages 376 – 396. The Royal Society, 1957.
- [16] G. Fagerlund. Relations between the strength and the degree of hydration or porosity of cement paste, cement mortar and concrete. Cementa report T87023, Danderyd, 1987.
- [17] C. Farhat and F.-X. Roux. A method of finite element tearing and interconnecting and its parallel solution algorithm. *International Journal for Numerical Methods in Engineering*, 32:1205–1227, 1991.
- [18] J. Fish and K. Shek. Multiscale analysis of composite materials and structures. *Composites Science and Technology*, 60(12-13):2547 – 2556, 2000.
- [19] S. Ghosh, J. Bai, and P. Raghavan. Concurrent multi-level model for damage evolution in microstructurally debonding composites. *Mechanics of Materials*, 39(3):241 – 266, 2007.
- [20] Z. C. Grasley and D. A. Lange. Constitutive modeling of the aging viscoelastic properties of portland cement paste. *Mech. Time-Depend Mater.*, 11:175–198, 2007.
- [21] Z. C. Grasley and D. A. Lange. The viscoelastic response of cement paste to three-dimensional loading. *Mech. Time-Depend Mater.*, 11:27–46, 2007.
- [22] Z. Hashin. The elastic moduli of heterogeneous materials. *Journal of Applied Mechanics*, 29:143–150, 1962.
- [23] T. Hettich, A. Hund, and E. Ramm. Modeling of failure in composites by X-FEM and level sets within a multiscale framework. *Comput. Methods Appl. Mech. Engrg.*, 197:414–424, 2009.
- [24] R. Hill. Theory of mechanical properties of fiber-strengthened materials - III: Self-consistent model. *J. Mech. Phys. Solids*, 13:189–198, 1965.
- [25] M. Hlobil, V. Šmilauer, and G. Chanvillard. Micromechanical multiscale fracture model for compressive strength of blended cement pastes. *Cement and Concrete Research*, 83:188 – 202, 2016.
- [26] A. Idiart. *Coupled analysis of degradation processes in concrete specimens at the meso-level*. Ph.D. Thesis, Universitat Politècnica de Catalunya, Barcelona, 2009.
- [27] L. Jendele, V. Šmilauer, and J. Červenka. Multiscale hydro-thermo-mechanical model for early-age and mature concrete structures. *Advances in Engineering Software*, 72:134–146, 2014.

-
- [28] M. Jirásek and Z. P. Bažant. *Inelastic analysis of structures*. John Wiley & Sons, Ltd., 2002.
- [29] S. Kamali, M. Moranville, E. G. Garboczi, S. Prené, and B. Gérard. Hydrate dissolution influence on the young's modulus of cement paste. In Li, , et al., editors, *Proc. Fracture Mechanics of Concrete Structures (FraMCoS-V)*, pages 631 – 638, Vail, 2004. Routledge.
- [30] T. Kanit, S. Forest, I. Galliet, V. Mounoury, and D. Jeulin. Determination of the size of the representative volume element for random composites: Statistical and numerical approach. *International Journal of Solids and Structures*, 40:3647–3679, 2003.
- [31] V. Kouznetsova, M. G. D. Geers, and W. A. M. Brekelmans. Multi-scale constitutive modelling of heterogeneous materials with a gradient-enhanced computational homogenization scheme. *Int. J. Numer. Meth. Engng.*, 54(8):1235–1260, 2002.
- [32] F. Lea. *Lea's Chemistry of Cement and Concrete*. Elsevier, fourth edition, 2004.
- [33] J. H. Lienhard and J. H. Lienhard. *A heat transfer textbook*. Phlogiston Press, Cambridge, 2008.
- [34] K. Maekawa, R. P. Chaube, and T. Kishi. *Modeling of Concrete Performance*. E & FN SPON (London), first edition, 1999.
- [35] J.-P. Mercier, W. Kurz, and G. Zambelli. *Introduction à la science des matériaux: Traité des matériaux - Volume 1*. Presses Polytechniques et Universitaires Romandes, 1989.
- [36] H. Moulinec and P. Suquet. A fast numerical method for computing the linear and non-linear mechanical properties of composites. *Comptes Rendus de l'Academie des Sciences Serie II*, 318(11):1417–1423, 1994.
- [37] National Ready Mixed Concrete Association. *Concrete in practice*. Technical report, NRMCA, 1978–2007.
- [38] A. M. Neville. *Properties of Concrete*. John Wiley & Sons, Inc., 1997.
- [39] M. Nilsson. *Thermal Cracking of Young Concrete. Partial Coefficients, Restraint Effects and Influence of Casting Joints*. Licentiate thesis, Luleå Univeristy of Technology, 2000.
- [40] J. Němeček, V. Králík, V. Šmilauer, L. Polívka, and A. Jäger. Tensile strength of hydrated cement paste phases assessed by micro-bending tests and nanoindentation. *Cement and Concrete Composites*, 2015. *submitted*.

-
- [41] J. Němeček, V. Šmilauer, and L. Kopecký. Nanoindentation characteristics of alkali-activated aluminosilicate materials. *Cement and Concrete Composites*, 33(2):163–170, 2011.
- [42] C. Pichler and R. Lackner. A multiscale creep model as basis for simulation of early-age concrete behavior. *Computers and Concrete*, 5(4):295 – 328, 2008.
- [43] T. C. Powers and T. L. Brownyards. Studies of physical properties of hardened portland cement paste. Bulletin 22, Research Laboratories of the Portland Cement Association, Chicago, March 1948.
- [44] P. Raghavan and S. Ghosh. Concurrent multi-scale analysis of elastic composites by a multi-level computational model. *Computer Methods in Applied Mechanics and Engineering*, 193(6-8):497 – 538, 2004.
- [45] RILEM Technical Committee TC-242-MDC (Z.P. Bažant, chair). Model B4 for creep, drying shrinkage and autogenous shrinkage of normal and high-strength concretes with multi-decade applicability (RILEM Technical Committee TC-242-MDC multi-decade creep and shrinkage of concrete: material model and structural analysis). *Materials and Structures*, 48:753–770, 2015.
- [46] P. E. Roelfstra. *Numerical concrete*. Ph.D. Thesis, EPFL, Lausanne, Switzerland, 1988.
- [47] I. Schrage and T. V. Summer. Factors influencing early cracking of high strength concrete. In R. Springenschmidt, editor, *Proceedings of International RILEM Symposium. Thermal Cracking in Concrete at Early Ages*, page 237–244, Munich, Germany, Oct 1994.
- [48] W. R. L. da Silva and Šmilauer. Fuzzy affinity hydration model. *Journal of Intelligent and Fuzzy Systems*, 28(1):127–139, 2015.
- [49] W. R. L. da Silva, V. Šmilauer, and P. Štemberk. Upscaling semi-adiabatic measurements for simulating temperature evolution of mass concrete structures. *Materials and Structures*, 48(4):188–197, 2015.
- [50] V. Šmilauer. *Multiscale hierarchical modeling of hydrating concrete*. Saxe-Coburg Publications, first edition, 2015.
- [51] V. Šmilauer, L. Baquerizo, T. Matschei, P. Havlásek, W. R. L. da Silva, and K. Hájková. Contemp – a virtual thermo-mechanical simulator for hydrating reinforced concrete blocks with extension to service life. In *International RILEM Conference on Materials, Systems and Structures in Civil Engineering*, 2016.

-
- [52] V. Šmilauer and Z. P. Bažant. Identification of viscoelastic C-S-H behavior in mature cement paste by FFT-based homogenization method. *Cem. Concr. Res.*, 40(2):197 – 207, 2010.
- [53] V. Šmilauer and Z. Bittnar. Microstructure-based micromechanical prediction of elastic properties in hydrating cement paste. *Cem. Concr. Res.*, 36(9):1708–1718, 2006.
- [54] V. Šmilauer, P. Hlaváček, Škvára F., Šulc R., L. Kopecký, and J. Němeček. Micromechanical multiscale model for alkali activation of fly ash and metakaolin. *Journal of Materials Science*, 46(20):6545–6555, 2012.
- [55] V. Šmilauer, C. G. Hoover, Z. P. Bažant, F. C. Caner, A. M. Waas, and K. W. Shahwan. Multiscale Simulation of Fracture of Braided Composites via Repetitive Unit Cells. *Engineering Fracture Mechanics*, 78(6):901–918, 2011.
- [56] V. Šmilauer and T. Krejčí. Multiscale Model for Temperature Distribution in Hydrating Concrete. *International Journal for Multiscale Computational Engineering*, 7(2):135–151, 2009.
- [57] J.-H. Song and T. Belytschko. Multiscale aggregating discontinuities method for micro-macro failure of composites. *Composites Part B: Engineering*, 40(6):417 – 426, 2009.
- [58] B. T. Tamtsia and J. J. Beaudoin. Basic creep of hardened cement paste. A re-examination of the role of water. *Cem. Concr. Res.*, 30:1465–1475, 2000.
- [59] H. F. W. Taylor. *Cement Chemistry*. Academic Press, New York, 1990.
- [60] P. D. Tennis and H. M. Jennings. A model for two types of calcium silicate hydrate in the microstructure of Portland cement pastes. *Cem. Concr. Res.*, 30:855–863, 2000.
- [61] J. Vorel, V. Šmilauer, and Z. Bittnar. Multiscale simulations of concrete mechanical tests. *Journal of Computational and Applied Mathematics*, 236(18):4882–4892, 2012.
- [62] B.-L. Wang and Y.-W. Mai. Transient one-dimensional heat conduction problems solved by finite element. *International Journal of Mechanical Sciences*, 47(2):303–317, 2005.
- [63] A. Zaoui. Continuum Micromechanics: Survey. *Journal of Engineering Mechanics*, 128(8):808 – 816, 2002.
- [64] T. Zohdi and P. Wriggers. A domain decomposition method for bodies with heterogeneous microstructure based on material regularization. *International Journal of Solids and Structures*, 36(17):2507 – 2525, 1999.